Neuron
Article

The Y Cell Visual Pathway Implements a Demodulating Nonlinearity

Ari Rosenberg[1,3,*] and Naoum P. Issa[2,4,*]
[1]Committee on Computational Neuroscience
[2]Department of Neurobiology
University of Chicago, Chicago, IL 60615, USA
[3]Present address: Department of Anatomy and Neurobiology, Washington University School of Medicine, St. Louis, MO 63110, USA (A.R.)
[4]Present address: Medical Resource Group, LLC, P.O. Box 15185, Chicago, IL 60615, USA (N.P.I.)
*Correspondence: rosenberg@pcg.wustl.edu (A.R.), naoumpissa@gmail.com (N.P.I.)
DOI 10.1016/j.neuron.2011.05.044

SUMMARY

Neural encoding of sensory signals involves both linear and nonlinear processes. Determining which nonlinear operations are implemented by neural systems is crucial to understanding sensory processing. Here, we ask if demodulation, the process used to decode AM radio signals, describes how Y cells in the cat LGN nonlinearly encode the visual scene. In response to visual AM signals across a wide range of carrier frequencies, Y cells were found to transmit a demodulated signal, with the firing rate of single-units fluctuating at the envelope frequency but not the carrier frequency. A comparison of temporal frequency tuning properties between LGN Y cells and neurons in two primary cortical areas suggests that Y cells initiate a distinct pathway that carries a demodulated representation of the visual scene to cortex. The nonlinear signal processing carried out by the Y cell pathway simplifies the neural representation of complex visual features and allows high spatiotemporal frequencies to drive cortical responses.

INTRODUCTION

The neural encoding of the visual scene involves both linear and nonlinear processing. Linear processing detects image features defined by spatiotemporal variation in luminance, and is typified by X cells in the retina and lateral geniculate nucleus (LGN) (Enroth-Cugell and Robson, 1966; Hochstein and Shapley, 1976; So and Shapley, 1979). Nonlinear processing is required to detect non-Fourier image features such as interference patterns, and begins subcortically with Y cells (Demb et al., 2001b; Rosenberg et al., 2010). Although it has long been established that Y cells respond nonlinearly to visual stimulation (Hochstein and Shapley, 1976), the nonlinear transformation they implement has not been determined. In this study, we ask whether Y cells implement a nonlinear signal processing technique called "demodulation."

Demodulation is a nonlinear process used to detect envelope frequencies in interference patterns. For instance, to decode an amplitude-modulated (AM) radio signal created by multiplying a high-frequency carrier by low-frequency envelopes to be communicated. Because there are no actual signal components at the envelope frequencies, their detection requires a nonlinear transformation of the input which is implemented by a demodulating circuit in the radio receiver. Interference patterns are also found abundantly in natural visual scenes, defining important features such as object contours (Johnson and Baker, 2004; Schofield, 2000; Song and Baker, 2007). Theoretical work suggests that demodulation could provide an efficient method for encoding visual interference patterns and other non-Fourier image features (Daugman and Downing, 1995; Fleet and Langley, 1994), but the existence of a neural mechanism for visual demodulation has only been speculated.

To determine if LGN Y cells transmit a demodulated visual signal, we examined the temporal pattern of their responses to interference patterns with different carrier temporal frequencies but the same envelope temporal frequency (TF). Y cell responses to these stimuli were found to be demodulated, oscillating at the envelope (but not the carrier) TF and with the same phase regardless of the carrier TF. To investigate if the demodulated signal transmitted by Y cells is represented in primary visual cortex, we compared the TF tuning properties of LGN Y cells with those of neurons in cortical areas 17 and 18. Like Y cells, area 18 neurons responded to interference patterns across a wide range of carrier TFs. This property could not be accounted for by the output of area 17 which represented a narrow range of low TFs. This suggests that Y cells initiate a distinct pathway that carries a demodulated representation of the visual scene to area 18. Envelope detection has now been observed in the periphery and subcortical nuclei of a number of sensory systems including the amphibian and mammalian auditory systems (Jaramillo et al., 1993; Shofner et al., 1996), the electric fish electrosensory system (Savard et al., 2011), and the mammalian visual system (Demb et al., 2001b; Rosenberg et al., 2010). Whether early mechanisms for envelope detection have analogous signal processing roles across sensory systems or perform unique functions in each system is an open question. In the visual system, we show that envelopes are detected by a subcortical demodulating nonlinearity that provides a number of advantages including: (1) creating an early representation of

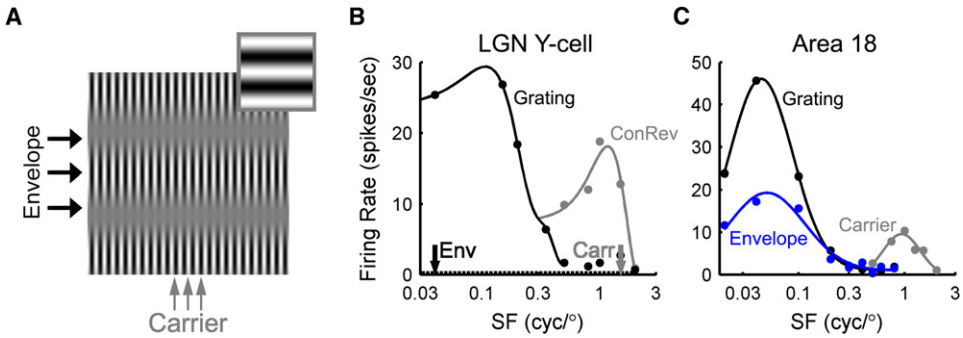

Figure 1. Example Interference Pattern and Spatial Frequency Tuning Curves of an LGN Y Cell and an Area 18 Neuron

(A) An interference pattern with a low SF horizontally oriented envelope (wide bands of alternating regions of low and high contrast) and a high SF vertically oriented carrier (fine sinusoidal modulation). Inset shows a miniature of the demodulated image, a low SF grating with the orientation and SF of the envelope.

(B) SF tuning curve of a Y cell. Y cells respond to low SF drifting gratings (black data points) and to high SF contrast-reversing gratings (gray data points). Data points are mean responses and the dashed line indicates baseline response. Solid curves are difference of Gaussians model fits. The envelope (Env) and carrier (Carr) SFs used to study this Y cell's responses to interference patterns were selected from these tuning curves, values marked with arrows.

(C) SF tuning curve of an area 18 neuron. Area 18 neurons respond to low SF drifting gratings (black data points), to interference patterns with low envelope SFs (blue data points) matching the drifting grating SFs, and to interference patterns with high carrier SFs (gray data points). Data points are baseline subtracted mean responses. Solid curves are log-Gaussian fits. The envelope SF tuning curve was measured with a carrier SF of 1.0 cyc/°. The carrier SF tuning curve was measured with an envelope SF of 0.04 cyc/°.

See also Figures S5 and S6.

complex visual features such as illusory contours, (2) providing cortex with information about higher spatiotemporal frequencies than is possible with known linear mechanisms, and (3) potentially establishing the foundation for the form-cue invariant processing of Fourier and non-Fourier image features. We propose that demodulation provides the basis for a conceptual framework describing how the Y cell pathway processes the visual scene, similar to how linear filtering provides a conceptual framework for the X cell pathway.

RESULTS

To investigate if the Y cell pathway encodes a demodulated visual signal, we recorded from three interconnected areas of the cat brain: the LGN, area 17, and area 18 (Humphrey et al., 1985; Price et al., 1994; Stone and Dreher, 1973). Y cells were recorded in the A and C layers of the LGN, where they were identified using a standard classification comparing responses to drifting and contrast-reversing gratings at different spatial frequencies (Hochstein and Shapley, 1976). Y cells respond linearly to low spatial frequency (SF) drifting gratings, oscillating at the stimulus TF. They respond nonlinearly to high SF contrast-reversing gratings, oscillating at twice the stimulus TF. Here, we examine if the nonlinear responses of Y cells to stimuli composed of multiple high SFs are the result of a demodulating nonlinearity. To investigate the cortical representation of the nonlinear Y cell output, we recorded from two primary visual areas, areas 17 and 18 (Humphrey et al., 1985; Stone and Dreher, 1973; Tretter et al., 1975).

The stimulus set included sinusoidal gratings that drifted or reversed in contrast as well as three-component interference patterns analogous to AM radio signals (Figure 1A; Equation 1). An interference pattern is constructed by summing three high SF sinusoidal gratings (a carrier frequency and two sidebands positioned symmetrically about the carrier in frequency space). Despite containing only high SFs, the stimulus elicits the perception of an oriented low SF pattern that corresponds to the envelope (see Figure 1 in Rosenberg et al., 2010). Whereas linear processing can detect each of the three grating components (the carrier and two sidebands), nonlinear processing is required to detect the envelope since it is not in the power spectrum of the stimulus (Daugman and Downing, 1995; Fleet and Langley, 1994). Importantly, the spatial parameters of the interference patterns were tailored to the individual Y cells and area 18 neurons so that none of the three grating components could elicit linear responses, necessarily making any observed response nonlinear. For each Y cell, the carrier SF was selected to be above the linear passband of the neuron's drifting grating SF tuning curve and near the nonlinear SF preference measured using contrast-reversing gratings (Rosenberg et al., 2010; Figure 1B). For each area 18 neuron, the carrier SF tuning curve was measured directly using SFs above the passband of the drifting grating SF tuning curve (Zhou and Baker, 1996; Figure 1C). Subsequent measurements used a carrier SF near the cell's preference. Because area 18 neurons that respond to non-Fourier image features show form-cue invariant tuning for the spatial parameters of drifting gratings and the envelopes of interference patterns (Figure 1C), the envelope orientation and SF were set near the linear preferences measured using drifting gratings for both Y cells and area 18 neurons (Rosenberg et al., 2010; Zhou and Baker, 1996). To ensure that only nonlinear responses were elicited, the carrier and envelope SFs were jointly constrained so that the SFs of the grating components were all too high to elicit linear responses (following Equation 1).

Previous work has shown that Y cells (but not X cells) respond to the envelope of interference patterns when the carrier is static (Demb et al., 2001b; Rosenberg et al., 2010). However, these

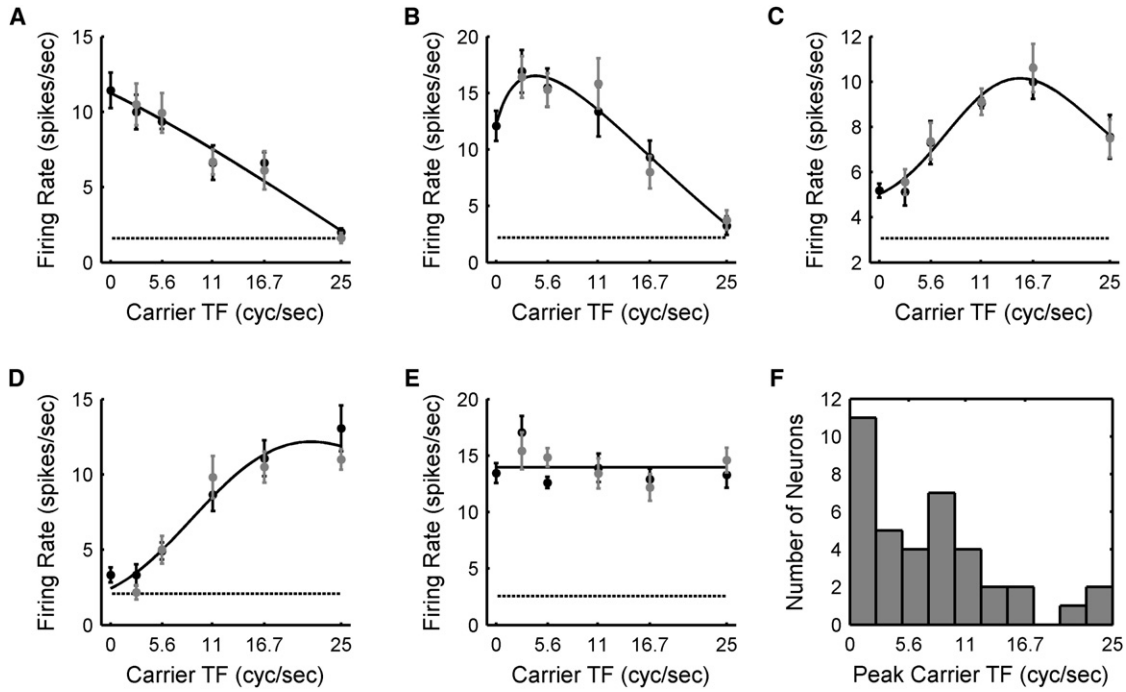

Figure 2. Y Cell Carrier Temporal Frequency Tuning Curves

(A–E) Carrier TF tuning curves of five Y cells. Gray and black data points are mean responses to carriers drifting in opposite directions. Dashed lines indicate baseline responses and error bars are SEM. Solid curves are gamma function fits in (A)–(D) and a horizontal line in (E). The carrier TF tuning curves in this figure were measured with an envelope TF of 5.6 cyc/s; carrier TF tuning curves measured at other envelope TFs were similarly shaped (see Figure S1).

(F) Histogram of peak carrier TFs for 38 Y cells. Data for 4 Y cells lacking a clear peak (as in E) were excluded from the histogram.

See also Figure S2.

studies could not identify the nonlinear transformation implemented by Y cells. To determine if Y cells implement a demodulating nonlinearity, we presented interference patterns with the same envelope TF but different carrier TFs. Because demodulation extracts the envelope and eliminates the carrier and other components (the sidebands) from the original signal, a demodulating nonlinearity will produce identical temporal responses to each of these stimuli; specifically, oscillating at the envelope TF and with the same phase. Nondemodulating nonlinearities will give rise to multiplicative interactions between the stimulus components which may generate responses at the envelope TF but which also introduce response frequencies that depend on the carrier TF. For instance, this is observed in the periphery of the auditory system, where distortion products at the envelope frequency and a number of carrier-dependent frequencies are introduced at the level of individual hair cells (Jaramillo et al., 1993).

Y Cell Carrier Temporal Frequency Tuning

If Y cells encode a demodulated visual signal, then their responses to interference patterns will oscillate at the envelope TF and with the same phase, regardless of the carrier TF. Previous studies have only characterized Y cell responses to interference patterns with a static carrier (Demb et al., 2001b; Rosenberg et al., 2010), so it was important to first determine the range of carrier TFs over which they respond. For each Y cell, a series of interference patterns was presented in which only the carrier TF was varied. The spatial parameters of the stimuli were tailored to match the tuning preferences of the cell being studied and the envelope TF was typically 5.6 cyc/s. The amplitude of Y cell responses to interference patterns was found to depend smoothly on carrier TF (Figures 2A–2D; see Figure S1 available online). The carrier TF tuning curves were diverse in shape and often broadly tuned. In a few instances, the response amplitude was almost completely invariant across the entire range of tested frequencies (Figure 2E). The majority of tuning curves (38/42) were well-described by a gamma function (average r = 0.91 ± 0.08 standard deviation [SD], n = 38). Tuning properties estimated from these fits are summarized in Table 1, and the distribution of peak carrier TFs is presented in Figure 2F. As a population, Y cells were found to respond well to interference patterns over a wide range of carrier TFs ranging from 0 to at least 25 cyc/s.

Y Cell Carrier Direction Selectivity

To determine if carrier TF tuning is affected by the carrier's direction of motion, carrier TF tuning curves were measured with the carrier drifting in opposite directions but with all other stimulus parameters the same (Figures 2A–2E). The two measurements were highly correlated (average r = 0.85 ± 0.18 SD, n = 42), indicating that the carrier's direction of motion has little effect on the shape of the carrier TF tuning curve. To quantify carrier direction

Table 1. Summary Table of Temporal Frequency Tuning Properties in the LGN and Cortical Areas 17 and 18

	Peak (cyc/s)	Left Half-Height (cyc/s)	Right Half-Height (cyc/s)	Bandwidth (octaves)
Y cells carrier	7.5 ± 6.8 n = 38	3.8 ± 3.6 n = 19	15.3 ± 5.8 n = 28	3.2 ± 1.4 n = 14
Area 18 carrier	6.2 ± 6.6 n = 17	3.6 ± 2.4 n = 5	11.1 ± 5.3 n = 15	2.6 ± 1.0 n = 4
Area 17 grating	3.5 ± 1.9 n = 43	1.2 ± 0.7 n = 31	8.3 ± 3.6 n = 43	3.0 ± 1.0 n = 31
Y cells envelope	4.0 ± 1.2 n = 30	1.7 ± 0.6 n = 30	9.0 ± 3.6 n = 30	2.4 ± 0.7 n = 30
Area 18 envelope[a]	3.8 ± 2.0 n = 30	—	—	1.8 ± 0.9 n = 23

Values are mean ± standard deviation. See also Figure S4.
[a] As reported in Mareschal and Baker (1998b).

selectivity, a direction tuning index (DTI) was calculated at the nonzero carrier TF that elicited the largest amplitude response (Equation 2). Values close to zero indicate no direction selectivity and values near one indicate strong direction selectivity. The measured DTI values were low, average DTI = 0.10 ± 0.09 SD (n = 42), indicating that Y cells respond about equally well to interference patterns with carriers drifting in opposite directions. The absence of carrier direction selectivity was confirmed in measurements of carrier orientation and direction tuning at the preferred carrier TF (Supplemental Text and Figure S2). Together, the high correlations and low DTI values indicate that the carrier's direction of motion has little effect on Y cell carrier TF tuning.

Frequency Analysis of Y Cell Responses to Interference Patterns

Having measured how the amplitude of Y cell responses to interference patterns depends on the carrier's TF and direction of motion, we next wanted to determine if the responses were demodulated. To do so, we examined the temporal pattern of Y cell responses to interference patterns with the same envelope TF but different carrier TFs. The responses of a linear system and a demodulating system to interference patterns are qualitatively different. If the component frequencies of an interference pattern are within the passband of a linear system, the output of that system will oscillate predominantly at the carrier TF (if the component frequencies are outside the passband there will be no response). In contrast, the output of a demodulating system will oscillate predominantly at the envelope TF and will not respond at the carrier or other component frequencies. Importantly, the frequency content in the output of a demodulating system will not depend on the carrier TF.

Responses to interference patterns could also result from nonlinear (multiplicative) interactions between the different component frequencies present in the stimulus. The possible nonlinear interactions are limited by the observation that Y cell responses to interference patterns with a static carrier contain power at the envelope TF and twice the envelope TF (Demb et al., 2001b; Rosenberg et al., 2010). The simplest nonlinear interaction that would explain this observation is the sum of pairwise multiplications of the component frequencies. In response to a three component interference pattern, this nonlinearity would produce five dominant response frequencies: (1) TF_{env}, (2) $2TF_{env}$, (3) $2TF_{carr}$, (4) $2TF_{carr} - TF_{env}$, and (5) $2TF_{carr} + TF_{env}$. Note that with a static carrier, the only response components are at TF_{env} and $2TF_{env}$, as previously observed experimentally. Nonlinear interactions such as these may result in responses at the envelope TF, but the responses are not demodulated since they also include a set of carrier-dependent output frequencies. For instance, carrier-dependent responses are observed in the output of individual hair cells in the peripheral auditory system (Jaramillo et al., 1993). Because the carrier was held static in previous Y cell experiments, demodulating and nondemodulating nonlinearities could not be differentiated. Importantly, the frequency content in the output of a non-demodulating nonlinear system will depend substantially on the carrier TF.

It is thus possible to differentiate a demodulating system from a linear or other nonlinear system by presenting interference patterns at different carrier TFs and examining the frequency content in the output. To determine the frequency content in Y cell responses to interference patterns, peristimulus time histograms (PSTHs) with 10 ms bins were constructed and mean subtracted. Power spectra were then computed from the fast Fourier transforms of the PSTHs and each power spectrum was normalized to have a maximum value of one. For each carrier TF, a population averaged power spectrum was then calculated using responses to interference patterns with the same envelope TF (5.6 cyc/s). Regardless of the carrier TF, the responses oscillated predominantly at the envelope TF (Figure 3). Progressively smaller but distinct peaks attributable to static (e.g., half-wave rectification and expansive) nonlinearities inherent to spiking neural responses were also observed at the second and third harmonics of the envelope TF. Similar response patterns were observed at both lower and higher envelope TFs (Figure S1). Thus, the frequency content in Y cell responses to interference patterns does not depend substantially on the carrier TF. This is consistent with a demodulating system and is inconsistent with either a linear system or a non-demodulating nonlinear system.

Frequency analysis showed that Y cell responses to interference patterns contain power at the envelope TF and its second and third harmonics. For some of the presented stimuli, either one or two of the three component gratings also drifted at these frequencies. For instance, when the carrier is held static as it was in previous studies (Demb et al., 2001b; Rosenberg et al., 2010) two of the components drift at the envelope TF. This overlap of frequency content is a confounding factor that can be eliminated by only considering responses to interference patterns if the three component TFs are different than the envelope TF and its second and third harmonics. Across our data set, a total of 124 responses to interference patterns matching this criterion were recorded from 24 Y cells. To further examine if these responses were consistent with the output of a demodulating system, the PSTHs were fit with two models: (1) a "linear model"—the sum of three sinusoids at the component TFs and (2) a "demodulated model"—the sum of three sinusoids at the envelope TF and its second and third harmonics (see Experimental Procedures for

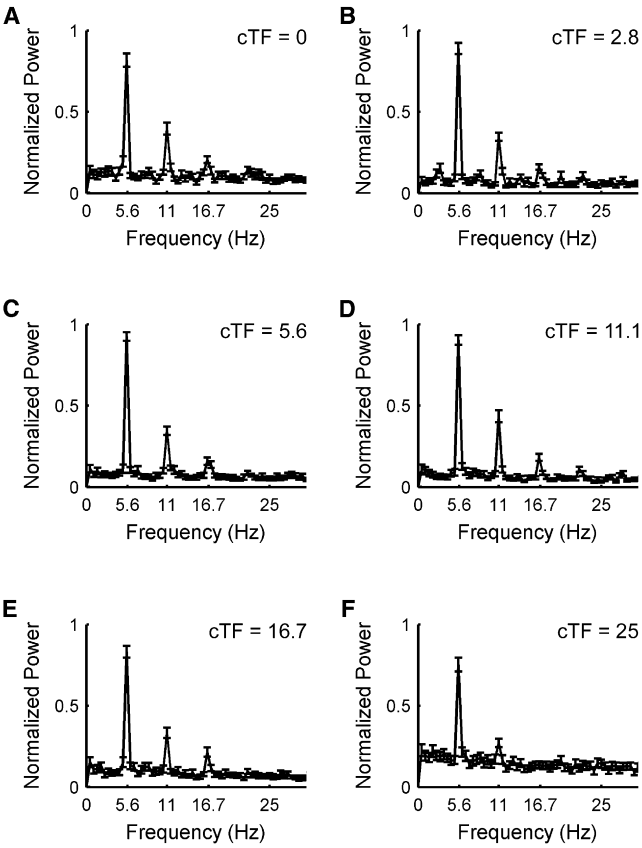

Figure 3. Power Spectra of Y Cell Responses to Interference Patterns

Average normalized power spectra of the responses of 33 Y cells measured at six different carrier TFs and an envelope TF of 5.6 cyc/s are presented. Distinct peaks are observed at the envelope TF and its second and third harmonics.

(A) Carrier TF (cTF) = 0 cyc/s.

(B) Carrier TF = 2.8 cyc/s.

(C) Carrier TF = 5.6 cyc/s.

(D) Carrier TF = 11.1 cyc/s.

(E) Carrier TF = 16.7 cyc/s.

(F) Carrier TF = 25 cyc/s.

Mean ± SEM plotted (n = 66 measurements per carrier TF, 33 Y cells times two carrier directions). The peaks at the envelope frequency are less than one because not all Y cells responded at every carrier TF.

See also Figures S1 and S5.

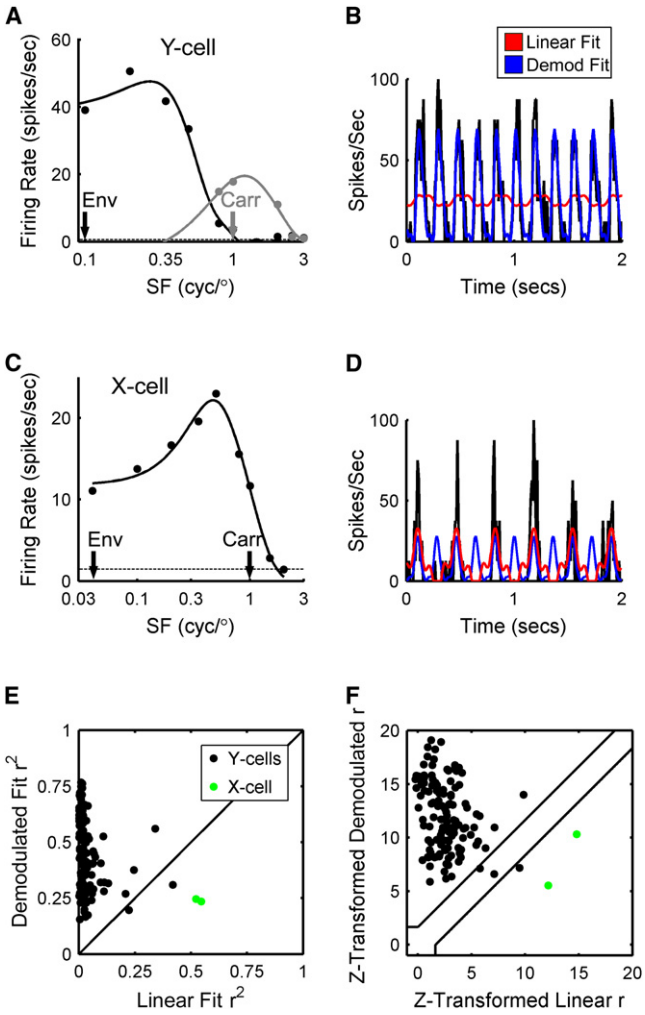

Figure 4. Demodulated and Linear Image Representations in the LGN

(A) SF tuning curve of a Y cell, layout as in Figure 1B. Arrows indicate the envelope and carrier SFs of the interference pattern that elicited the response shown in (B).

(B) Example demodulated (blue trace) and linear (red trace) fits to a Y cell response to an interference pattern with a carrier TF (cTF) of 2.8 cyc/s and an envelope TF of 5.6 cyc/s ($Z_{Dem} - Z_{Lin} = 17.88$).

(C) SF tuning curve of an X cell measured using drifting gratings. Data points are mean responses and the dashed line indicates baseline response. Solid curve is the difference of Gaussians model fit. Arrows indicate the envelope and carrier SFs of the interference pattern that elicited the response shown in (D).

(D) Example demodulated (blue trace) and linear (red trace) fits to an X cell response to an interference pattern with a carrier TF of 2.8 cyc/s and an envelope TF of 5.6 cyc/s ($Z_{Dem} - Z_{Lin} = -6.61$).

(E) Scatter plot of the accounted variance (r^2) between the PSTHs and the linear and demodulated fits (n = 124 Y cell measurements and 2 X cell measurements). Diagonal line is unity.

(F) Z-scored partial correlations of the data shown in (E). The diagonally running boundary lines demarcate responses classified as demodulated (upper left region), unclassified (intermediate region), and linear (lower right region).

See also Figures S3 and S5.

details). The SF tuning and interference pattern parameter selections for a Y cell along with an example PSTH with linear and demodulated model fits are shown in Figures 4A and 4B. To compare the quality of the fits and to classify the responses as either "linear" or "demodulated," partial correlations were computed between the PSTHs and model fits and then converted into Z scores using Fisher's r-to-Z transformation (see Experimental Procedures). This transformation normalizes correlations so that their difference may be used as an index quantifying model performance (Smith et al., 2005). For each cell, the difference between the Z-scored demodulated fit (Z_{Dem}) and Z-scored linear fit (Z_{Lin}) was taken ($Z_{Dem} - Z_{Lin}$) such that a positive value indicates that the demodulated model

outperformed the linear model and a negative value indicates that the linear model outperformed the demodulated model. On average, $Z_{Dem} - Z_{Lin}$ = 9.41 ± 4.15 SD (N = 124 measurements from 24 Y cells), indicating that the demodulated model provided a significantly better description of Y cell responses than the linear model. Of the 124 Y cell measurements, 121 were classified as demodulated, 2 were unclassified, and 1 was classified as linear (Figures 4E and 4F). For comparison, the same analysis was performed on the responses of an A-layer X cell to interference patterns with component SFs within its passband (Figures 4C and 4D). Consistent with X cells performing a linear analysis of the visual scene (Enroth-Cugell and Robson, 1966; Hochstein and Shapley, 1976; Victor et al., 1977), the X cell responded predominantly at the carrier TF and its responses were classified as linear ($Z_{Dem} - Z_{Lin} = -5.55$, average of two measurements). Highlighting that the X cell and Y cell pathways provide distinct parallel representations of the visual scene, this X cell and a Y cell simultaneously recorded on the same electrode encoded qualitatively different image features over a similar range of spatiotemporal frequencies (Figure S3).

Phase Analysis of Y Cell Responses to Interference Patterns

Consistent with the output of a demodulating system, the frequency content in Y cell responses to interference patterns was found to not depend on the carrier TF. Because the phase of the envelope does not depend on the carrier TF, the phase of a demodulating system's responses to interference patterns does not depend on the carrier TF either. To further test if Y cell responses to interference patterns are consistent with the output of a demodulating system, we next examined if response phase depends on the carrier TF. For each interference pattern to which a Y cell responded, the response phase was estimated by constructing a PSTH with 10 ms bins and then fitting the PSTH with a sinusoid fixed at the envelope TF. The amplitude and phase of the sinusoid were free parameters and the fitted phase value was used as the estimate of response phase. An example Y cell carrier TF tuning curve along with PSTHs and sinusoidal fits for three carrier TFs are shown in Figures 5A–5D (same cell as in Figures 4A and 4B). For this cell, the estimated response phases did not vary greatly with the carrier TF (SD = 8.6°, n = 11). To determine the extent to which response phase varied with carrier TF across the population, the estimated response phases for each Y cell were transformed into relative response phases by subtracting their mean. For example, if a Y cell responded to three interference patterns and the estimated response phases were 39°, 40°, and 41° (mean = 40°), then the relative response phases for that cell were −1°, 0°, and 1°, respectively. The population histogram of relative response phases (n = 354 measurements from 42 Y cells) had an empirical SD of 14.3° and was well described by a Gaussian (r = 0.99) centered at −0.4° with a SD of 10.9° (Figure 5E), indicating that response phase did not vary greatly with carrier TF. Importantly, the narrow distribution of relative response phases was not the result of a narrow distribution of estimated response phases, which was about 3.4 times broader (empirical SD = 48.9°). The distributions of relative and estimated (recentered at 0°) response phases were significantly different ($p < 0.0001$, Kolmogorov-Smirnov test). To determine if changing the carrier TF resulted in a small but systematic change in response phase across the population, the mean and 95% confidence interval of the relative response phases was calculated for each carrier TF (Figure 5F). For every carrier TF, 0° was within the 95% confidence interval of the mean relative response phase, and a Runs test for randomness did not reveal a significant trend between carrier TF and relative response phase ($p > 0.99$, n = 11).Thus, the phase of Y cell responses to interference patterns does not depend substantially on the carrier TF. This finding is consistent with a demodulating system.

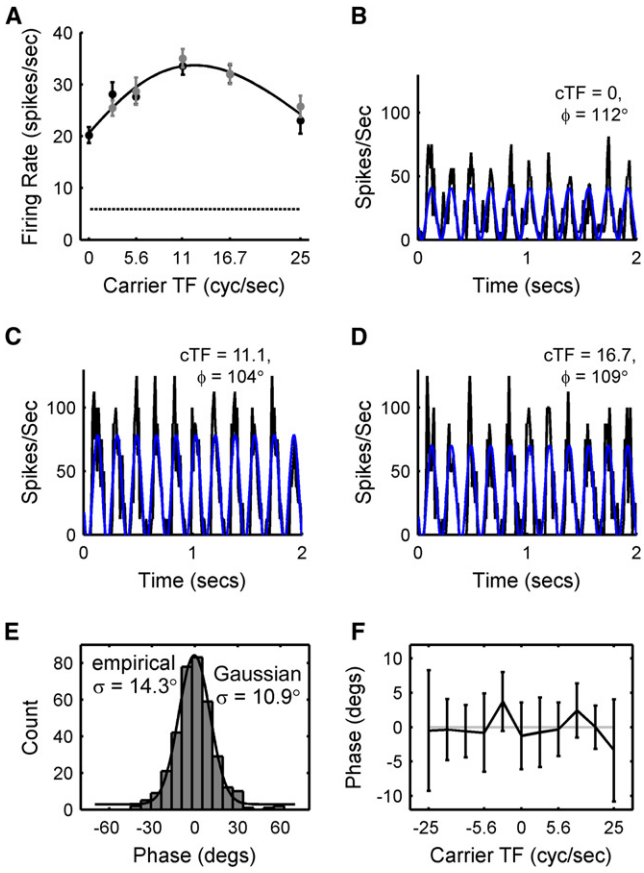

Figure 5. Y Cell Responses to Interference Patterns Are Phase Locked to the Envelope

(A) Y cell carrier TF tuning curve measured with an envelope TF of 5.6 cyc/s, layout as in Figure 2. Error bars show SEM. The SF tuning and SF parameter selections for this cell are shown in Figure 4A.

(B–D) PSTHs at three carrier TFs (black traces) and sinusoidal fits at the envelope TF (blue traces clipped at zero). The carrier TF (cTF) of the stimulus and the phase (ϕ) of the fitted sinusoid is shown for each PSTH. Regardless of the carrier TF, responses oscillated at the envelope TF and approximately the same phase. The response at a fourth carrier TF (2.8 cyc/s; $\phi = 110°$) is shown in Figure 4B.

(E) Histogram of the relative response phases of 354 measurements from 42 Y cells. The phases were narrowly distributed with a Gaussian profile.

(F) Across the population, the relative response phase shows no trend with carrier TF. Mean relative phases and 95% confidence intervals plotted. From left to right, the number of measurements was: 22, 31, 38, 35, 36, 30, 36, 35, 38, 31, and 22.

Y Cell Responses to Illusory Contours

Theoretical work has shown that a demodulating nonlinearity will detect a variety of non-Fourier image features including illusory contours (ICs) (Daugman and Downing, 1995; Fleet and Langley, 1994). By extension, our finding that Y cells demodulate interference patterns led us to hypothesize that they will respond to other non-Fourier image features as well. To test this, abutting grating stimuli that produce ICs detected by some neurons in the primary visual cortex of cats and monkeys were drifted across the receptive fields of three LGN Y cells (Grosof et al., 1993; Song and Baker, 2007; Figure S4A). Importantly, the spatial parameters of the stimuli were tailored to the individual Y cells to ensure that only nonlinear responses could be elicited. Specifically, the carrier SF was selected to be above the linear passband of the neuron's drifting grating SF tuning curve and near the nonlinear SF preference measured using contrast-reversing gratings. The ICs were also constrained to be oriented orthogonally to the carrier to ensure that spatial harmonics in the stimulus did not fall within the linear passband of the cell. Even with the small sample size, the result of this experiment was clear: the responses of all three Y cells oscillated at the frequency of ICs/sec, indicating that the ICs were detected (Figures S4B and S4C). Responses at this frequency are consistent with the output of a demodulating system and cannot be explained by linear processing since a linear response would oscillate at half this frequency. This result suggests that by demodulating visual signals, Y cells may encode a variety of complex image features.

Comparisons of Y Cell Temporal Frequency Tuning Properties

Because the amplitude of Y cell responses to interference patterns depends on both the envelope TF (Rosenberg et al., 2010) and the carrier TF (Figure 2), we next wanted to compare the representations of envelope and carrier TF based on response amplitude. Envelope TF tuning curves were measured with a static carrier for 30 Y cells. These tuning curves were well-described by gamma functions (average r = 0.94 ± 0.04 SD) which were used to estimate the tuning properties summarized in Table 1. For 24 of these Y cells, we also measured a carrier TF tuning curve that was well-described by a gamma function. The envelope and carrier TF tuning curves of a Y cell along with a population scatter plot of the peak envelope TFs and peak carrier TFs are shown in Figures S5A and S5B. Whereas the peak envelope TFs of these 24 Y cells were narrowly distributed around a low frequency (4.2 cyc/s ± 1.2 SD), the peak carrier TFs were widely distributed around a higher frequency (7.5 cyc/s ± 6.8 SD). The distributions of peak envelope TFs and peak carrier TFs were significantly different ($p = 0.005$, Mann-Whitney U test), and there was a moderate but nonsignificant correlation between them ($r = 0.36$, $p = 0.08$). The sensitivity of Y cells to a restricted range of low envelope TFs is consistent with results from cat area 18 (Mareschal and Baker, 1998b) and human psychophysical studies (Derrington and Cox, 1998; Smith and Ledgeway, 1998). Their sensitivity to high carrier TFs is also consistent with results from cat area 18 which we describe in the next section and human psychophysical studies (D'Antona and Shevell, 2009; Stockman and Plummer, 1998).

We also found no significant relationship between the peak grating TFs (measured using drifting gratings at the peak grating SF) and peak carrier TFs of Y cells. The grating and carrier TF tuning curves of a Y cell along with a population scatter plot of the peak grating TFs and peak carrier TFs are shown in Figures S5C and S5D.

Comparisons of Subcortical and Cortical Temporal Frequency Tuning Properties

If Y cells initiate a pathway that carries a demodulated representation of the visual scene, then there must be downstream cortical processing of this nonlinear representation. To explore this, we recorded from area 18 which receives direct input from LGN Y cells (Humphrey et al., 1985; Stone and Dreher, 1973). Many area 18 neurons respond to interference patterns (Zhou and Baker, 1996), but it is debated whether these responses reflect the processing of subcortical Y cell input or cortical area 17 input (Demb et al., 2001b; Mareschal and Baker, 1998a; Rosenberg et al., 2010). We address this question further by examining the selectivity of area 18 neurons for carrier TF and asking whether the tuning properties are better explained by input from Y cells or area 17.

Consistent with our Y cell measurements and data from a previous study that measured carrier TF tuning in a small sample of area 18 neurons (Zhou and Baker, 1996), we found that area 18 carrier TF tuning curves were diverse in shape and often broadly tuned (Figure 6). The tuning curves were also well-described by gamma functions (average r = 0.94 ± 0.04 SD, n = 17). Using these fits to estimate tuning properties (Table 1), we found that area 18 carrier TF tuning curves were similar to those of LGN Y cells. The distributions of Y cell peak carrier TFs and area 18 peak carrier TFs were not significantly different (Kolmogorov-Smirnov test, $p = 0.40$; Figure 7A). The Y cell right half-heights were significantly greater than the area 18 right half-heights (two-sample t test, $p = 0.01$), but the two distributions were highly overlapping (Figure 7B). The population of area 18 neurons, like the Y cell population, represented the entire range of tested carrier TFs. Area 18 carrier TF tuning curves measured with the carrier drifting in opposite directions were also similar in shape (average r = 0.90 ± 0.10 SD, n = 17) and carrier direction selectivity was low (average DTI = 0.14 ± 0.10 SD, n = 17). The distributions of Y cell carrier DTI values and area 18 carrier DTI values were not significantly different (Kolmogorov-Smirnov test, $p = 0.25$). These results are consistent with the hypothesis that area 18 responses to interference patterns reflect the processing of Y cell input (Demb et al., 2001b; Rosenberg et al., 2010).

That the carrier TF tuning of LGN Y cells and area 18 neurons is similar suggests that area 18 constructs its sensitivity to interference patterns from the output of LGN Y cells. Another possibility is that area 18 constructs its sensitivity to interference patterns from the output of area 17 (Mareschal and Baker, 1998a), which is linear in the sense that it represents the individual grating components of complex stimuli (Zhang et al., 2007). To investigate this possibility, we measured grating TF tuning curves from area 17 neurons using drifting gratings at their peak orientation, direction, and SF. The tuning curves were well described by gamma functions (average r = 0.96 ± 0.04 SD, n = 43) which

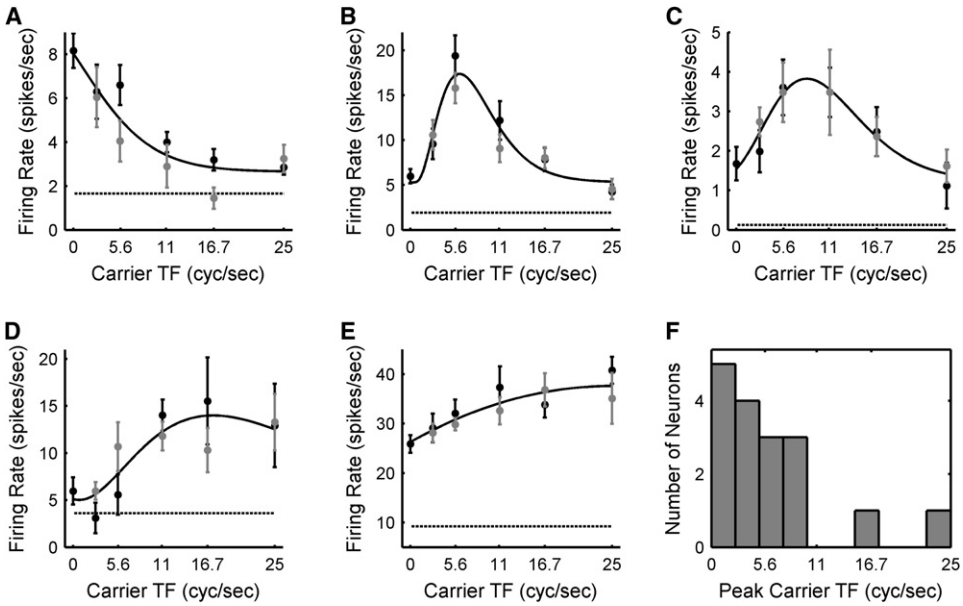

Figure 6. Area 18 Carrier Temporal Frequency Tuning Curves

(A–E) Carrier TF tuning curves of five area 18 neurons. Gray and black points are mean responses to carriers drifting in opposite directions. Dashed lines indicate baseline responses and error bars are SEM. Solid curves are gamma function fits. (A, D, and E) Measured with an envelope TF of 5.6 cyc/s. (B and C) Measured with an envelope TF of 2.8 cyc/s.

(F) Histogram of peak carrier TFs for 17 area 18 neurons.

were used to estimate the tuning properties summarized in Table 1. These measurements provide an estimate of the TFs represented in the output of cat area 17 and are similar to those reported in previous studies (Ikeda and Wright, 1975; Movshon et al., 1978). However, if there is lowpass temporal filtering between the input and output layers of cat area 17, as there is in the primate (Hawken et al., 1996), our measurements may overestimate the high TF cutoff of the area 17 output because the cellular layers of the recording sites were not identified. Even with this potential overestimate, the output of area 17 was found to represent a narrow range of low grating TFs that could not account for the high carrier TF cutoff of area 18 neurons (Figures 7A and 7B). The distributions of area 17 peak grating TFs and area 18 peak carrier TFs were significantly different (Kolmogorov-Smirnov test, $p = 0.05$). More importantly, the area 18 carrier TF right half-heights were significantly greater than the area 17 grating TF right half-heights (two-sample t test, $p = 0.01$), suggesting that the output of area 17 cannot underlie many of the interference pattern responses recorded in area 18. These results further support the hypothesis that area 18 responses to interference patterns reflect the processing of Y cell input.

DISCUSSION

Demodulation is a signal analysis technique used to extract information transmitted through the envelopes of interference patterns. Visual interference patterns are highly prevalent in natural scenes (Johnson and Baker, 2004; Schofield, 2000), and their representation along with other non-Fourier image features has been linked to the detection of object contours and texture patterns (Rivest and Cavanagh, 1996; Song and Baker, 2007). Theoretical work suggests that demodulation is an efficient way to encode non-Fourier image features (Daugman and Downing, 1995; Fleet and Langley, 1994), but a neural mechanism for visual demodulation has not been identified. Although previous studies have demonstrated that Y cells respond to interference patterns with a static carrier, the nonlinear transformation implemented by Y cells could not be identified (Demb et al., 2001b; Rosenberg et al., 2010). To determine if the nonlinear responses of Y cells are the result of a demodulating

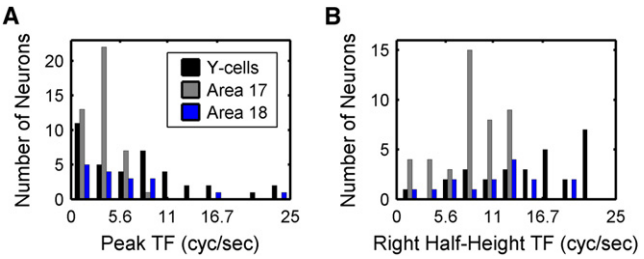

Figure 7. Comparison of LGN Y Cell/Area 18 Carrier Temporal Frequency Tuning and Area 17 Grating Temporal Frequency Tuning

(A) Peak carrier TFs of LGN Y cells (n = 38) and area 18 neurons (n = 17), and peak grating TFs of area 17 neurons (n = 43). The Y cell data are the same as in Figure 2F, and the area 18 data are the same as in Figure 6F.

(B) Carrier TF tuning curve right half-heights of LGN Y cells (n = 28) and area 18 neurons (n = 15), and grating TF tuning curve right half-heights of area 17 neurons (n = 43).

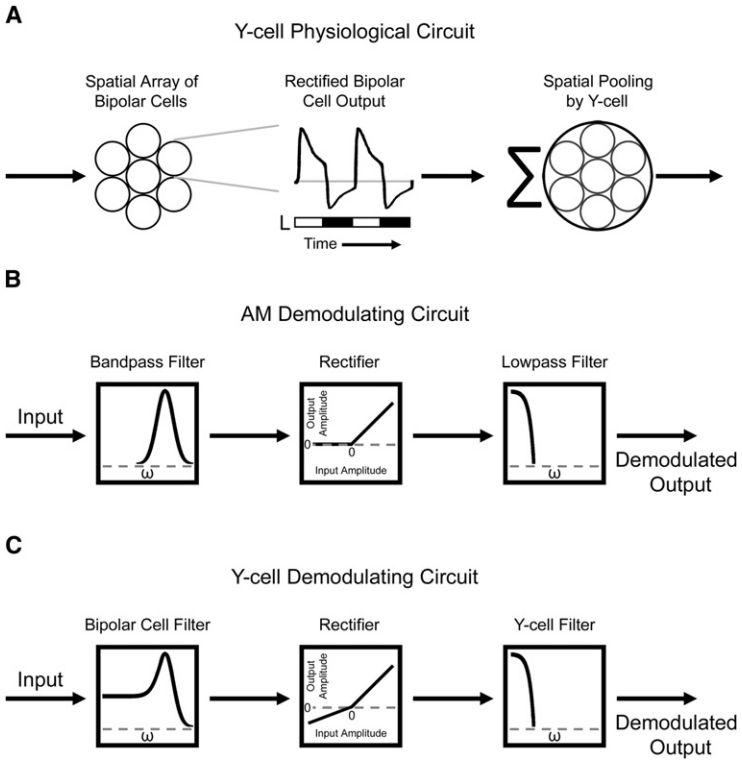

Figure 8. Demodulating Circuits

(A) Schematic of the physiological circuit producing the center region of a retinal ganglion Y cell receptive field. (1) Bipolar cells presynaptic to retinal ganglion Y cells have small center-surround receptive fields which respond preferentially to high SFs but also respond to low SFs (Dacey et al., 2000). (2) These bipolar cells respond more strongly to luminance of one sign than to the other, so their responses are partially rectified (Dacey et al., 2000). (3) The output of a spatial array of these bipolar cells is pooled by a retinal ganglion Y cell.

(B) Schematic of an AM radio demodulating circuit. The circuit can be summarized in three stages: (1) the input signal is linearly filtered with a first-stage bandpass filter centered on the high carrier frequency and which completely eliminates low frequencies, (2) in the second-stage the filtered output is rectified, and (3) the transformed signal is linearly filtered with a third-stage lowpass filter.

(C) The physiology of retinal ganglion Y cells also implements a demodulating circuit that can be summarized in three stages: (1) the input signal is linearly filtered with a first-stage (bipolar cell) filter that emphasizes high SFs and attenuates low SFs, (2) the filtered output is rectified in the second stage by a nonlinearity that compresses signal values of one sign, and (3) the transformed signal is linearly filtered with a third-stage (Y cell) lowpass filter.

nonlinearity, interference patterns were presented at multiple carrier TFs, and the frequency content and phase of the responses analyzed. Responses oscillated predominantly at the envelope TF and with the same phase regardless of the carrier TF. Importantly, the frequency content of the responses did not depend on the carrier TF. This pattern of responses is consistent with a demodulating system, but not a linear system or a nondemodulating nonlinear system. To investigate if there is downstream cortical processing of this demodulated representation, we recorded from cortical areas 17 and 18. The carrier TF tuning properties of area 18 neurons were highly similar to those of LGN Y cells and could not be fully accounted for by the output of area 17, suggesting that an anatomically and functionally distinct pathway begins with retinal ganglion Y cells, projects to LGN Y cells, and then to area 18.

A Physiological Circuit for Demodulating the Visual Scene

In this section, we describe how the physiological circuitry of retinal ganglion Y cells might implement visual demodulation. The circuit is schematized with a three-stage model of the Y cell spatial receptive field center (Figure 8A). The structure of this model is similar to a "pooled subunits model" of retinal ganglion Y cells (Enroth-Cugell and Freeman, 1987) and is supported by in vitro work showing that the nonlinear responses of retinal ganglion Y cells are largely attributable to their bipolar cell input (Crook et al., 2008; Dacey et al., 2000; Demb et al., 2001a). In the first stage, a visual input is processed by bipolar cells with small center-surround receptive fields that are maximally sensitive to high SFs. In the second stage, the bipolar cell output is subjected to a nonlinear transformation that partially rectifies the output, resulting in larger amplitude responses to luminance of one sign than to luminance of the other sign (Dacey et al., 2000). In the third stage, a retinal ganglion Y cell pools the output of bipolar cells whose receptive fields are adjacent in retinotopic space, resulting in the large center region of the Y cell receptive field that is maximally sensitive to low SFs.

This physiological circuitry parallels the traditional demodulating circuit used in AM radio, and both circuits can be summarized with similar three-stage filtering models (Figures 8B and 8C). In the first stage, the AM radio demodulating circuit linearly filters an input signal over a passband centered on the high carrier frequency. Similarly, bipolar cell processing can be described by a linear filter that is maximally sensitive to high SFs and which attenuates low SFs (Dacey et al., 2000). In the second stage, the AM radio demodulating circuit rectifies the output of the linear filter, which introduces the envelope frequencies. Similarly, the nonlinearity that partially rectifies the output of bipolar cells will introduce envelope frequencies. In the third stage, the AM radio demodulating circuit linearly filters the transformed signal with a lowpass filter to eliminate high frequencies, leaving only the envelope frequencies. Similarly, the Y cell pooling of a spatial array of bipolar cells acts like lowpass filtering, thereby eliminating high SFs. These parallels indicate how the physiological circuitry of retinal ganglion Y cells might implement visual demodulation.

Carrier Temporal Frequency Tuning

LGN Y cells and area 18 neurons were found to be tuned for the carrier TF of interference patterns, but the origin of this tuning remains an open question. One possibility is that it originates retinally, perhaps reflecting the TF tuning of bipolar cells. However, this may not be the case since a Y cell's grating TF

tuning will depend on the TF tuning of its bipolar cell input, and there was no correlation between the peak grating TFs and peak carrier TFs of LGN Y cells (Figure S5D). In addition, we found that some LGN Y cells do not respond to interference patterns with a static carrier, but there is no indication that such Y cells are found in the retina (Demb et al., 2001b), although this may reflect a species difference. An interesting possibility is that carrier TF tuning emerges in the LGN. It has been argued that there is a large proliferation of Y cells between the retina and LGN, much greater than that of X cells (Friedlander et al., 1981), and this proliferation may in part reflect the introduction of carrier TF tuning.

Individual LGN Y cells and area 18 neurons were found to be broadly tuned for carrier TF, indicating that they extract envelope information over a spectrally broad domain. This broadband carrier selectivity may have advantages over narrowband carrier selectivity for image processing (Daugman and Downing, 1995). Moreover, the diversity in the shape of the carrier TF tuning curves (Figures 2 and 6) implies that envelope information originating from different carrier TF bands will differentially activate the neural population. Because of this, it should be possible to decode envelope information at specific carrier TFs at the population level. It will be interesting for future studies to determine the extent to which envelope information originating within different carrier bands is combined or segregated by the visual system.

The Origin of the Cortical Representation of Non-Fourier Image Features

There are two active hypotheses regarding how the cortical representation of non-Fourier image features arises in the cat. One hypothesis is that these nonlinear responses are constructed in area 18 from the output of area 17 (Mareschal and Baker, 1998a). Consistent with major theories of early visual processing, this model argues that subcortical X cells encode a linear representation of the visual scene that is projected to cortical area 17 where further linear processing is performed (Issa et al., 2008; Zhang et al., 2007). The model then posits a nonlinear operation performed in area 18 on the output of area 17 which produces the representation of non-Fourier image features (Mareschal and Baker, 1998a). This may thus be considered an X cell pathway model for constructing a neural representation of non-Fourier image features. Alternatively, it has been hypothesized that the sensitivity of area 18 neurons to non-Fourier image features originates with a preexisting neural representation created by retinal ganglion Y cells (Demb et al., 2001b; Rosenberg et al., 2010). Critical to this model is that cat area 18 is a primary visual area, receiving substantial input from LGN Y cells (Humphrey et al., 1985; Stone and Dreher, 1973). This may thus be considered a Y cell pathway model for constructing a neural representation of non-Fourier image features. Here we showed that both Y cells and area 18 neurons represent interference patterns over a wide range of carrier TFs (at least as high as 25 cyc/s). Importantly, the sensitivity of area 18 neurons to interference patterns with high carrier TFs could not be accounted for by the output of area 17 which represents a narrower range of low TFs (Figure 7). Our findings are thus most consistent with the Y cell pathway model, supporting the hypothesis that the cortical representation of non-Fourier image features is constructed from Y cell input.

Implications of Visual Demodulation

The functional advantages of a demodulating nonlinearity in communication and signal processing have been revealed through a variety of engineering applications. The finding that Y cells implement a demodulating nonlinearity helps to draw parallels between Y cell physiology and traditional demodulating circuits and suggests that demodulation can provide the basis for a conceptual framework for understanding the role of the Y cell pathway in visual processing. In this final section, we introduce some implications of a Y cell demodulating nonlinearity.

Implication 1. Reducing the Statistical Complexity of Neural Representations

Non-Fourier image features are defined by high-order correlations describing how different sinusoidal components in an image come in and out of phase (Klein and Tyler, 1986). This statistical complexity implies a greater computational expense in representing non-Fourier image features than simpler image features defined solely by changes in luminance. It would consequently be more efficient to represent non-Fourier image features after transforming them into a neural representation with less statistical complexity. Demodulation performs this transformation, recoding complex spatiotemporal patterns composed of multiple high-frequency components into a simpler form that represents the lower spatiotemporal scale at which those components covary, the envelope frequency (Figures 3–5). Importantly, this transformation preserves the salient image features (the envelope information) and encodes/transmits them more efficiently (Daugman and Downing, 1995). The present results therefore suggest that the Y cell pathway reduces the statistical complexity and improves the efficiency of neural representations of complex visual features.

Implication 2. Form-Cue Invariant Processing

Although they are similar, there are important differences between the Y cell demodulating circuit and the traditional demodulating circuit used in AM radio. One major difference is that the AM radio rejects low-input frequencies whereas Y cells (and area 18 neurons) respond linearly to low SF drifting gratings (Figures 1B and 1C). It is consequently important to explain how Y cells can demodulate visual signals yet still respond linearly to low SF drifting gratings. This difference between the circuits can be traced to their first-stage filters. In the AM radio, the first-stage filter completely eliminates low frequencies, whereas the first-stage filter in the Y cell circuit (describing the filtering properties of bipolar cells) largely attenuates but still passes low SFs (Dacey et al., 2000) (c.f., Figures 8B and 8C). The third-stage filter in either circuit only passes low frequencies (whether they are in the input signal or introduced because of rectification in the second stage). Since the first-stage filter in the AM radio circuit completely eliminates low input frequencies, the third-stage filter can only pass low frequencies introduced because of rectification. On the other hand, the first-stage filter in the Y cell circuit only attenuates low SFs in the input signal, so the third-stage filter (describing the Y cell spatial pooling of

bipolar cells) passes both a linear representation of low SFs present in the input and a nonlinear (demodulated) representation of low SFs introduced because of the rectification of complex patterns comprised of high SFs.

The first-stage filter settings in the Y cell circuit may be functionally significant for visual processing since they result in a Y cell output with properties area 18 neurons can use to construct form-cue invariant responses. Form-cue invariance refers to the similar tuning of area 18 neurons for the spatial parameters of drifting gratings and the envelopes of interference patterns (Zhou and Baker, 1996; Figure 1C). This invariance has previously been explained using a cortically-inspired model that posits the convergence of distinct linear and nonlinear processing "streams" (Baker and Mareschal, 2001). The nonlinear stream detects non-Fourier image features using a circuit that is similar to an AM radio in that the first-stage filter completely eliminates low SFs. For the model to also respond to gratings, a converging linear stream with filter settings matching the third-stage filter in the nonlinear stream is required. A more parsimonious model explaining both sets of responses with a single processing stream is achieved with the Y cell demodulating circuit (Figures 8A and 8C). The Y cell demodulating circuit produces purely demodulated responses when the visual input contains multiple high SFs, dominantly linear responses when it contains only low SFs, and mixed responses when it contains intermediate SFs (c.f., Hochstein and Shapley, 1976; Victor et al., 1977). The Y cell output consequently contains both the linear and nonlinear response components necessary for area 18 neurons to produce form-cue invariant responses, which can be implemented in the model by a fourth stage that linearly filters the Y cell output with an oriented filter selective for low SFs. Thus, one advantage of a subcortical demodulating nonlinearity is that it simplifies the construction of a form-cue invariant circuit.

Implication 3. Subcortical Encoding of Illusory Contours

Like many other nonlinear scene representations, the neural representation of ICs has been thought to originate in cortex (Baker and Mareschal, 2001; Song and Baker, 2007; von der Heydt and Peterhans, 1989). However, since theoretical work has shown that a demodulating nonlinearity will detect ICs (Daugman and Downing, 1995), we hypothesized that a neural representation of ICs may originate subcortically with Y cells. To examine this possibility, we recorded the responses of a small number of LGN Y cells to abutting grating stimuli used to study cortical processing of ICs (Grosof et al., 1993; Song and Baker, 2007). Y cell responses invariably oscillated at the frequency of ICs/s, indicating that the ICs were detected (Figure S4). This suggests that by demodulating visual signals, Y cells may encode a variety of complex image features whose detection was previously thought to require cortical processing.

Implication 4. Bypassing the Lowpass Geniculocortical Temporal Filter

Neural responses to high spatiotemporal frequencies are significantly attenuated between the LGN and primary visual cortex (Derrington and Fuchs, 1979; Hawken et al., 1996; Ikeda and Wright, 1975; Movshon et al., 1978). This lowpass filtering in the geniculocortical transformation is thought to limit the perception of dynamic visual scenes (Hawken et al., 1996; Zhang et al., 2007). For example, the imperceptible flicker of 60 Hz monitor refresh drives many subcortical but few cortical neurons (Wollman and Palmer, 1995). However, by extracting envelope TFs subcortically, high spatiotemporal frequencies that are filtered out in the geniculocortical transformation may still influence perception. Consider the invariant carrier TF tuning of the cell shown in Figure 2E. Whether the component TFs are low or high, the signal transmitted to cortex is indistinguishable (it oscillates at the envelope TF). Because only low envelope TFs are represented by Y cells (Table 1; Figure S5B), they are not filtered out in the geniculocortical transformation. As such, a cortical neuron innervated by this cell should have also responded to the motion of the envelope without regard to the carrier TF. Other Y cells, like the one in Figure 2D, only project information about interference patterns to cortex when the component frequencies are so high that it is unlikely that the envelope TF can be computed in cortex (i.e., from the output of area 17). This implies that image components whose spatiotemporal frequencies are too high to pass the geniculocortical filter can still drive cortical responses, and as a result, likely influence perception. This is consistent with psychophysical results showing that color perception is influenced by an interference pattern even when the component TFs are too high to be seen on their own (Stockman and Plummer, 1998). Similarly, in the phenomenon of induction, in which a temporally varying surround region induces an illusory modulation of a constant center region, the perceived modulation depth of the center is significantly attenuated at high surround TFs. However, when two high TFs are summed and presented in the surround, the center is perceived to modulate at the envelope frequency (D'Antona and Shevell, 2009). The present results thus suggest that a subcortical demodulating nonlinearity allows high TF information that is otherwise lost in the geniculocortical transformation to affect cortical firing patterns, and possibly perception.

Implication 5. Monocular Depth Cues

Non-Fourier signals are generally associated with the detection of oriented contours and the processing of texture (Rivest and Cavanagh, 1996; Song and Baker, 2007), but they also arise at occlusion boundaries and under conditions producing transparent motion (Fleet and Langley, 1994). Both occlusion boundaries and transparent motion, the perception of multiple velocity signals in a local area of retinotopic space (Qian and Andersen, 1994), provide monocular cues for depth order. Non-Fourier signals can consequently elicit salient depth perceptions from non-stereoscopic stimuli (Hegdé et al., 2004); for instance, the envelope of an interference pattern can be perceived to drift in front of the carrier (Fleet and Langley, 1994; Figure S6). The tuning of Y cells for both the envelope TF and the carrier TF of interference patterns (Figures S5A and S5B) therefore constitutes a joint representation of motions occupying an overlapping area of retinotopic space that can be perceived to be at different depths. Although the processing of occlusion boundaries and transparent motion is commonly associated with extrastriate cortex (Qian and Andersen, 1994; Rosenberg et al., 2008), the results of the present study suggest that some aspects of these signals are first represented subcortically.

EXPERIMENTAL PROCEDURES

Animal Preparation

All procedures were approved by the University of Chicago Institutional Animal Care and Use Committee. These methods have been described previously (Rosenberg et al., 2010; Zhang et al., 2007) and are summarized here. All experiments were performed in anesthetized adult female cats. Baytril (2.5–5 mg/kg SQ) was given as prophylaxis against infection, dexamethasone (1–2 mg/kg SQ) was given to reduce cerebral edema, and atropine (0.04 mg/kg SQ) was given to decrease tracheal secretions. Ophthalmic atropine (1%) and phenylephrine (10%) were instilled in the eyes to dilate the pupils and retract the nictitating membrane, respectively. Lactated Ringer's Solution (LRS) with 2.5% dextrose was delivered IV at a rate of 2–10 ml/kg/hr. Pancuronium bromide (0.1 mg/kg loading dose, 0.04–0.125 mg/kg/hr continuous) was given IV as a paralytic and delivered in the LRS. In the LGN experiments, anesthesia was induced using a mixture of ketamine (15 mg/kg) and acepromazine (0.05 mg/kg) given IM and supplemented with isoflurane. Anesthesia was maintained using isoflurane (1%–2%). In the cortical experiments, anesthesia was induced using thiopental (20-30 mg/kg IV) and also maintained using thiopental (either 2–3 mg/kg IV as needed or given at a continuous rate of 2–4 mg/kg/hr IV delivered in saline and supplemented as needed). Core temperature was continuously monitored and maintained around 38°C with either a heating pad or a water heating blanket. Positive pressure ventilation (1:2 O_2:N_2O) was adjusted to maintain end-tidal CO_2 between 3.8% and 5.0% with a peak inspiratory pressure of 10–21 cm H_2O. ECG and EEG were monitored throughout the experiment. Contact lenses were used to focus the eyes at a distance of 40 cm.

Electrophysiology

Single-unit extracellular action potentials were recorded using 0.5–10 MΩ epoxy-coated tungsten electrodes (FHC Inc., Bowdoin, ME). Action potentials were amplified and filtered at 5 kHz (A-M Systems, Model 1800, Carlsborg, WA), digitally sampled at either 10 or 20 kHz, and stored for off-line spike-sorting (CED, Micro 1400, Cambridge, England).

To record from the LGN, electrodes were lowered dorsoventrally through a craniotomy (Horsley-Clarke coordinates ~9 mm lateral and ~6 mm anterior). The LGN was identified during recording sessions by its stereotyped layer structure as well as by the physiological properties of individual neurons. Y cells were recorded from the A layers and the superficial portion of the C layer (n = 42). Area 17 was identified functionally using the optically imaged area 17–18 border defined by a shift from high to low SF preference running from the caudolateral portion to the rostromedial portion of the lateral gyrus (Zhang et al., 2007). The activity of 43 area 17 neurons was recorded. Drifting sinusoidal gratings were used to classify cells as simple or complex. Simple cells respond to drifting sinusoidal gratings with a larger modulation at the stimulus TF than in the DC offset of the response (F1/F0 $\geq$ 1), whereas complex cells respond with a larger DC offset (F1/F0 < 1). Of the area 17 cells recorded, 16 were classified as simple and 27 were classified as complex. Since it appears that both types of cells project from area 17 to area 18 (Price et al., 1994), we analyzed the area 17 simple and complex cell data together. Area 18 was targeted stereotaxically (Horsley-Clarke coordinates ~4 mm lateral and ~3 mm anterior). The activity of 17 area 18 neurons was recorded. Of the area 18 cells recorded, 4 were classified as simple and 13 were classified as complex. Data from some of these cells were presented in previous studies (Rosenberg et al., 2010; Zhang et al., 2007).

Visual Stimuli

Visual stimuli were generated by computer and displayed monocularly on a gamma-corrected CRT monitor with a mean luminance of either 26 or 27.5 cd/m^2 using the Psychophysics Toolbox extensions for MATLAB (The MathWorks, Natick, MA) (Brainard, 1997). The linear relationship between stimulus intensity commanded by the software and the output luminance of the monitor was confirmed in two ways: (1) with a light meter (Konica Minolta, Model LS-100, Tokyo, Japan) and (2) by performing a fast Fourier transform on visual stimuli photographed with a Dalsa 1M30 CCD camera (Dalsa Corporation, Waterloo, Ontario, Canada) (Rosenberg et al., 2010; Zhang et al., 2007). Stimuli were viewed from 40 cm and presented as full screen images on a 40 × 30 cm CRT monitor with a pixel resolution of 800 × 600 and a refresh rate of 100 Hz. Stimuli consisted of high contrast (80% Michelson) drifting or contrast-reversing sinusoidal gratings as well as three-component interference patterns (Equation 1; Figure 1A). In this equation, ω_C is the vector defining the carrier spatiotemporal frequencies, ω_E is the vector defining the envelope spatiotemporal frequencies, and χ is the vector defining the space and time dimensions (x,y,t). When measuring interference pattern responses with a drifting carrier, the carrier and envelope TFs were constrained to be whole multiples of each other. Without this constraint, the computation time and memory resources to construct and save the stimuli would have been too prohibitive to tailor the stimuli to the cell being studied. Fixing the carrier and envelope TFs to be whole multiples of each other meant constructing only one cycle of each stimulus (at most 36 frames) rather than a unique frame for each refresh of the monitor (200 frames per stimulus; the 100 Hz monitor refresh rate times the 2 s stimulus duration). Stimuli were presented statically for either 250 ms or 1 s before drifting for a period lasting 1, 2, or 3 s. Firing rates were calculated over the drift duration. Each stimulus was presented between 4 and 12 times. Baseline activity was measured during the presentation of gray screens whose luminance matched the mean luminance of the other stimuli.

$$\begin{aligned} I(x,y,t) &= \cos(\omega_C \cdot \chi) + 0.5 \cdot \{\cos([\omega_C - \omega_E] \cdot \chi) + \cos([\omega_C + \omega_E] \cdot \chi)\} \\ &= \cos(\omega_C \cdot \chi) \cdot [1 + \cos(\omega_E \cdot \chi)] \end{aligned} \quad (1)$$

Analysis

SF tuning was measured using between 5 and 9 stimuli. The SFs of the sinusoidal gratings, which were presented either in isolation or as components of contrast-reversing gratings or interference patterns, could range between 0.02 and 4.0 cyc/°, but rarely exceeded 3.0 cyc/°. The component SFs of the interference patterns did not exceed 2.0 cyc/°. In the LGN experiments, SF tuning curves were fit with difference of Gaussians (Enroth-Cugell and Robson, 1966). In the cortical experiments, SF tuning curves were fit with log-Gaussians.

TF tuning was measured using either 6 or 9 stimuli. The TFs of the sinusoidal gratings, which were either presented in isolation or as components of contrast-reversing gratings or interference patterns, typically ranged between 0 and 25 cyc/s. One component of the interference patterns with a carrier TF of 25 cyc/s was higher (25 cyc/s + the envelope TF). To estimate tuning properties, TF tuning curves were fit with gamma functions. If the maximum response was elicited at either 0 or 25 cyc/s, then that value was taken to be the preference. Because tuning curves were not extrapolated, half-heights and bandwidths were not always defined.

Carrier direction selectivity was assessed using the carrier TF tuning curve data. A direction tuning index (DTI) was calculated at the non-zero carrier TF that elicited the largest amplitude response, comparing baseline subtracted responses when the carrier drifted in opposite directions (R_{TF} and R_{-TF}) and all other parameters were the same (Equation 2):

$$DTI = \frac{R_{TF} - R_{-TF}}{R_{TF} + R_{-TF}} \quad (2)$$

A DTI near 0 indicates weak direction selectivity whereas a DTI near 1 indicates strong direction selectivity.

Classification of a neural response to an interference pattern as either "linear" or "demodulated" was performed using a correlation-based analysis. First, the PSTH of the neural response was constructed using 10 ms bins. Second, linear and demodulated models with equal numbers of parameters were fit to the PSTH using a least-squares algorithm (MATLAB). For the linear model, the PSTH was fit with the sum of three sinusoids whose TFs matched the three sinusoidal components comprising the interference pattern (ω_{c-e}, ω_c, and ω_{c+e}). For the demodulated model, the PSTH was fit with the sum of three sinusoids whose TFs matched the stimulus envelope TF and its second and third harmonics (ω_e, ω_{2e}, and ω_{3e}). The choice of frequencies for the demodulated model was based on the analysis presented in Figure 3, which revealed responses at the envelope frequency and its second and third harmonics. Importantly, there was no TF that appeared in both the linear and demodulated models. The phase and amplitudes of the fitted sinusoids were free parameters. To eliminate negative firing rates, the fits were half-wave rectified

after the fitting procedure was completed. Third, partial correlations between the PSTH and the two rectified fits were computed (Equation 3).

$$R_{Dem} = \frac{r_{Dem} - r_{Lin} r_{Mods}}{\sqrt{(1 - r_{Lin}^2)(1 - r_{Mods}^2)}} \qquad R_{Lin} = \frac{r_{Lin} - r_{Dem} r_{Mods}}{\sqrt{(1 - r_{Dem}^2)(1 - r_{Mods}^2)}} \quad (3)$$

R_{Dem} is the partial correlation between the PSTH and the demodulated fit. R_{Lin} is the partial correlation between the PSTH and the linear fit. The value r_{Dem} is the correlation between the PSTH and the demodulated fit, r_{Lin} is the correlation between the PSTH and the linear fit, and r_{Mods} is the correlation between the two model fits. Fourth, to directly compare the performance of the two models, the partial correlations were transformed using Fisher's r-to-Z transformation (Equation 4).

$$Z_{Dem} = \frac{\sqrt{N-3}}{2} \ln\left(\frac{1 + R_{Dem}}{1 - R_{Dem}}\right) \qquad Z_{Lin} = \frac{\sqrt{N-3}}{2} \ln\left(\frac{1 + R_{Lin}}{1 - R_{Lin}}\right) \quad (4)$$

N is the number of bins in the PSTH. Classification used a significance criterion of 1.645, equivalent to p = 0.05. Thus, for a response to be classified as demodulated, Z_{Dem} had to exceed Z_{Lin} (or 0 if Z_{Lin} was negative) by 1.645. Likewise, for a response to be classified as linear, Z_{Lin} had to exceed Z_{Dem} (or 0 if Z_{Dem} was negative) by 1.645. If neither of these conditions were met, the response was left unclassified.

SUPPLEMENTAL INFORMATION

Supplemental Information includes six figures and Supplemental Text and can be found with this article online at doi:10.1016/j.neuron.2011.05.044.

ACKNOWLEDGMENTS

We thank T. Robert Husson, Atul K. Mallik, and Jing Zhang for assistance during experimental sessions. This work was supported by Department of Homeland Security Fellowship DE-AC05-00OR22750 and Dissertation Grant DE-AC05-06OR23100 (A.R.) and grants from the Brain Research Foundation and Mallinckrodt Foundation (N.P.I.).

Accepted: May 27, 2011
Published: July 27, 2011

REFERENCES

Baker, C.L., Jr., and Mareschal, I. (2001). Processing of second-order stimuli in the visual cortex. Prog. Brain Res. *134*, 171–191.

Brainard, D.H. (1997). The Psychophysics Toolbox. Spat. Vis. *10*, 433–436.

Crook, J.D., Peterson, B.B., Packer, O.S., Robinson, F.R., Troy, J.B., and Dacey, D.M. (2008). Y cell receptive field and collicular projection of parasol ganglion cells in macaque monkey retina. J. Neurosci. *28*, 11277–11291.

D'Antona, A.D., and Shevell, S.K. (2009). Induced temporal variation at frequencies not in the stimulus: evidence for a neural nonlinearity. J. Vis. *9*, 1–11.

Dacey, D., Packer, O.S., Diller, L., Brainard, D., Peterson, B., and Lee, B. (2000). Center surround receptive field structure of cone bipolar cells in primate retina. Vision Res. *40*, 1801–1811.

Daugman, J.G., and Downing, C.J. (1995). Demodulation, predictive coding, and spatial vision. J. Opt. Soc. Am. A Opt. Image Sci. Vis. *12*, 641–660.

Demb, J.B., Zaghloul, K., Haarsma, L., and Sterling, P. (2001a). Bipolar cells contribute to nonlinear spatial summation in the brisk-transient (Y) ganglion cell in mammalian retina. J. Neurosci. *21*, 7447–7454.

Demb, J.B., Zaghloul, K., and Sterling, P. (2001b). Cellular basis for the response to second-order motion cues in Y retinal ganglion cells. Neuron *32*, 711–721.

Derrington, A., and Cox, M. (1998). Temporal resolution of dichoptic and second-order motion mechanisms. Vision Res. *38*, 3531–3539.

Derrington, A.M., and Fuchs, A.F. (1979). Spatial and temporal properties of X and Y cells in the cat lateral geniculate nucleus. J. Physiol. *293*, 347–364.

Enroth-Cugell, C., and Freeman, A.W. (1987). The receptive-field spatial structure of cat retinal Y cells. J. Physiol. *384*, 49–79.

Enroth-Cugell, C., and Robson, J.G. (1966). The contrast sensitivity of retinal ganglion cells of the cat. J. Physiol. *187*, 517–552.

Fleet, D.J., and Langley, K. (1994). Computational analysis of non-Fourier motion. Vision Res. *34*, 3057–3079.

Friedlander, M.J., Lin, C.S., Stanford, L.R., and Sherman, S.M. (1981). Morphology of functionally identified neurons in lateral geniculate nucleus of the cat. J. Neurophysiol. *46*, 80–129.

Grosof, D.H., Shapley, R.M., and Hawken, M.J. (1993). Macaque V1 neurons can signal 'illusory' contours. Nature *365*, 550–552.

Hawken, M.J., Shapley, R.M., and Grosof, D.H. (1996). Temporal-frequency selectivity in monkey visual cortex. Vis. Neurosci. *13*, 477–492.

Hegdé, J., Albright, T.D., and Stoner, G.R. (2004). Second-order motion conveys depth-order information. J. Vis. *4*, 838–842.

Hochstein, S., and Shapley, R.M. (1976). Quantitative analysis of retinal ganglion cell classifications. J. Physiol. *262*, 237–264.

Humphrey, A.L., Sur, M., Uhlrich, D.J., and Sherman, S.M. (1985). Termination patterns of individual X- and Y cell axons in the visual cortex of the cat: projections to area 18, to the 17/18 border region, and to both areas 17 and 18. J. Comp. Neurol. *233*, 190–212.

Ikeda, H., and Wright, M.J. (1975). Spatial and temporal properties of 'sustained' and 'transient' neurones in Area 17 of the cat's visual cortex. Exp. Brain Res. *22*, 363–383.

Issa, N.P., Rosenberg, A., and Husson, T.R. (2008). Models and measurements of functional maps in V1. J. Neurophysiol. *99*, 2745–2754.

Jaramillo, F., Markin, V.S., and Hudspeth, A.J. (1993). Auditory illusions and the single hair cell. Nature *364*, 527–529.

Johnson, A.P., and Baker, C.L., Jr. (2004). First- and second-order information in natural images: a filter-based approach to image statistics. J. Opt. Soc. Am. A Opt. Image Sci. Vis. *21*, 913–925.

Klein, S.A., and Tyler, C.W. (1986). Phase discrimination of compound gratings: generalized autocorrelation analysis. J. Opt. Soc. Am. A *3*, 868–879.

Mareschal, I., and Baker, C.L., Jr. (1998a). A cortical locus for the processing of contrast-defined contours. Nat. Neurosci. *1*, 150–154.

Mareschal, I., and Baker, C.L., Jr. (1998b). Temporal and spatial response to second-order stimuli in cat area 18. J. Neurophysiol. *80*, 2811–2823.

Movshon, J.A., Thompson, I.D., and Tolhurst, D.J. (1978). Spatial and temporal contrast sensitivity of neurones in areas 17 and 18 of the cat's visual cortex. J. Physiol. *283*, 101–120.

Price, D.J., Ferrer, J.M., Blakemore, C., and Kato, N. (1994). Functional organization of corticocortical projections from area 17 to area 18 in the cat's visual cortex. J. Neurosci. *14*, 2732–2746.

Qian, N., and Andersen, R.A. (1994). Transparent motion perception as detection of unbalanced motion signals. II. Physiology. J. Neurosci. *14*, 7367–7380.

Rivest, J., and Cavanagh, P. (1996). Localizing contours defined by more than one attribute. Vision Res. *36*, 53–66.

Rosenberg, A., Wallisch, P., and Bradley, D.C. (2008). Responses to direction and transparent motion stimuli in area FST of the macaque. Vis. Neurosci. *25*, 187–195.

Rosenberg, A., Husson, T.R., and Issa, N.P. (2010). Subcortical representation of non-Fourier image features. J. Neurosci. *30*, 1985–1993.

Savard, M., Krahe, R., and Chacron, M.J. (2011). Neural heterogeneities influence envelope and temporal coding at the sensory periphery. Neuroscience *172*, 270–284.

Schofield, A.J. (2000). What does second-order vision see in an image? Perception *29*, 1071–1086.

Shofner, W.P., Sheft, S., and Guzman, S.J. (1996). Responses of ventral cochlear nucleus units in the chinchilla to amplitude modulation by low-frequency, two-tone complexes. J. Acoust. Soc. Am. *99*, 3592–3605.

Smith, A.T., and Ledgeway, T. (1998). Sensitivity to second-order motion as a function of temporal frequency and eccentricity. Vision Res. *38*, 403–410.

Smith, M.A., Majaj, N.J., and Movshon, J.A. (2005). Dynamics of motion signaling by neurons in macaque area MT. Nat. Neurosci. *8*, 220–228.

So, Y.T., and Shapley, R. (1979). Spatial properties of X and Y cells in the lateral geniculate nucleus of the cat and conduction veolcities of their inputs. Exp. Brain Res. *36*, 533–550.

Song, Y., and Baker, C.L., Jr. (2007). Neuronal response to texture- and contrast-defined boundaries in early visual cortex. Vis. Neurosci. *24*, 65–77.

Stockman, A., and Plummer, D.J. (1998). Color from invisible flicker: a failure of the Talbot-Plateau law caused by an early 'hard' saturating nonlinearity used to partition the human short-wave cone pathway. Vision Res. *38*, 3703–3728.

Stone, J., and Dreher, B. (1973). Projection of X- and Y cells of the cat's lateral geniculate nucleus to areas 17 and 18 of visual cortex. J. Neurophysiol. *36*, 551–567.

Tretter, F., Cynader, M., and Singer, W. (1975). Cat parastriate cortex: a primary or secondary visual area. J. Neurophysiol. *38*, 1099–1113.

Victor, J.D., Shapley, R.M., and Knight, B.W. (1977). Nonlinear analysis of cat retinal ganglion cells in the frequency domain. Proc. Natl. Acad. Sci. USA *74*, 3068–3072.

von der Heydt, R., and Peterhans, E. (1989). Mechanisms of contour perception in monkey visual cortex. I. Lines of pattern discontinuity. J. Neurosci. *9*, 1731–1748.

Wollman, D.E., and Palmer, L.A. (1995). Phase locking of neuronal responses to the vertical refresh of computer display monitors in cat lateral geniculate nucleus and striate cortex. J. Neurosci. Methods *60*, 107–113.

Zhang, J.X., Rosenberg, A., Mallik, A.K., Husson, T.R., and Issa, N.P. (2007). The representation of complex images in spatial frequency domains of primary visual cortex. J. Neurosci. *27*, 9310–9318.

Zhou, Y.X., and Baker, C.L., Jr. (1996). Spatial properties of envelope-responsive cells in area 17 and 18 neurons of the cat. J. Neurophysiol. *75*, 1038–1050.

Neuron, Volume *71*

Supplemental Information

The Y Cell Visual Pathway Implements a Demodulating Nonlinearity

Ari Rosenberg and Naoum P. Issa

Inventory of Supplemental Materials

Supplemental Text. This is text describing "carrier orientation and direction selectivity" results and the methods used to calculate selectivity. The data in this section supports one of the findings (that Y-cells lack direction selectivity for the carrier), but is not the main result of the manuscript.

Main Figure 1.

Supplemental Figure 6 *The perception of an interference pattern.* This supplemental figure describes one of the ways drifting interference patterns, like that first introduced in Main Figure 1, are perceived. This is used in the discussion section to help explain one of the functional implications of demodulation by the Y-cell pathway.

Main Figure 2.

Supplemental Figure 2 *Y-cell carrier orientation and direction tuning.* Main Figure 2 characterizes how Y-cell responses to interference patterns depend on the carrier TF; this supplemental figure characterizes how the responses depend on the carrier's orientation and direction of motion.

Main Figure 3.

Supplemental Figure 1 *Y-cell responses to interference patterns with envelope temporal frequencies other than 5.6 cyc/sec.* The analysis in Main Figure 3 was conducted using only Y-cell responses to interference patterns with an envelope TF of 5.6 cyc/sec. This supplemental figure shows that the result presented in Main Figure 3 generalizes to other envelope TFs.

Main Figure 4.

Supplemental Figure 3 *Spatiotemporal frequency tuning of a simultaneously recorded X-cell and Y-cell.* This supplemental figure shows the unique example in our data set of an X-cell and a Y-cell recorded simultaneously on a single electrode, and is used to help illustrate the physiological differences between X-cells and Y-cells shown in Main Figure 4.

Main Figures 1, 3, and 4.

Supplemental Figure 5 *Y-cell responses to illusory contours.* This supplemental figure shows that Y-cells respond to illusory contours (another type of non-Fourier stimulus), and that their responses to illusory contours are qualitatively similar to their responses to interference patterns (shown in Main Figures 1, 3, and 4). These results show that the findings presented in the main text are not specific to just interference patterns, and are used in the discussion section to demonstrate one of the functional implications of demodulation by the Y-cell pathway.

Main Table.

Supplemental Figure 4 *Comparisons of Y-cell temporal frequency tuning properties.* This supplemental figure displays the weak or absent correlations among Y-cell TF tuning properties tabulated in the Main Table.

Y-cell Carrier Orientation and Direction Selectivity

The dependency of Y-cell responses on the carrier was further examined by measuring carrier orientation and direction tuning curves at the peak carrier TF (**Supplemental Figure 2A**). Carrier orientation selectivity was assessed using a circular variance measure, V_{OR} (supplemental equation 1), for which zero indicates that a cell responded equally well to all orientations and one indicates that it responded to a single orientation. On average, $V_{OR} = 0.16 \pm 0.03$ SEM (N = 31), indicating that Y-cells can show some selectivity for the carrier's orientation (**Supplemental Figure 2B**). Similar selectivity was observed when only a static carrier was used (Rosenberg et al., 2010). For Y-cells preferring a non-zero carrier TF, carrier direction selectivity was assessed using a circular variance measure, V_{DIR} (supplemental equation 2), for which zero indicates that a cell responded equally well to all directions of motion and one indicates that it responded to a single direction. On average, $V_{DIR} = 0.04 \pm 0.01$ SEM (N = 21), confirming the DTI analysis showing that Y-cells are largely insensitive to the carrier's direction of motion (**Supplemental Figure 2B**). LGN Y-cells can thus show some selectivity for the orientation of both static and drifting carriers, but they are poorly selective for the carrier's direction of motion.

Supplemental Experimental Procedures

Carrier orientation and direction tuning curves were measured using interference patterns at the preferred carrier TF. The stimuli differed only in the orientation and direction of the carrier, and typically either 8 static carrier orientations or 8 carrier orientations x 2 drift directions were presented. Carrier orientation selectivity was quantified after baseline subtracting the data using a circular variance measure with a π-periodic polar space (V_{OR}; supplemental equation 1):

Supplemental equation 1: $$V_{OR} = \left| \frac{\sum_i R_i \exp(i2\theta_i)}{\sum_i R_i} \right|$$

The response at orientation θ_i is given by R_i. A V_{OR} of 0 indicates that a neuron responded equally well to all orientations whereas a V_{OR} of 1 indicates that a neuron responded to a single orientation.

Carrier direction selectivity was quantified after baseline subtracting the data using a circular variance measure with a 2π-periodic polar space (V_{DIR}; supplemental equation 2):

Supplemental equation 2: $$V_{DIR} = \left| \frac{\sum_i R_i \exp(i\theta_i)}{\sum_i R_i} \right|$$

The response at direction θ_i is given by R_i. A V_{DIR} of 0 indicates that a neuron responded equally well to all directions of motion whereas a V_{DIR} of 1 indicates that a neuron responded to a single direction.

Supplemental Figure 1

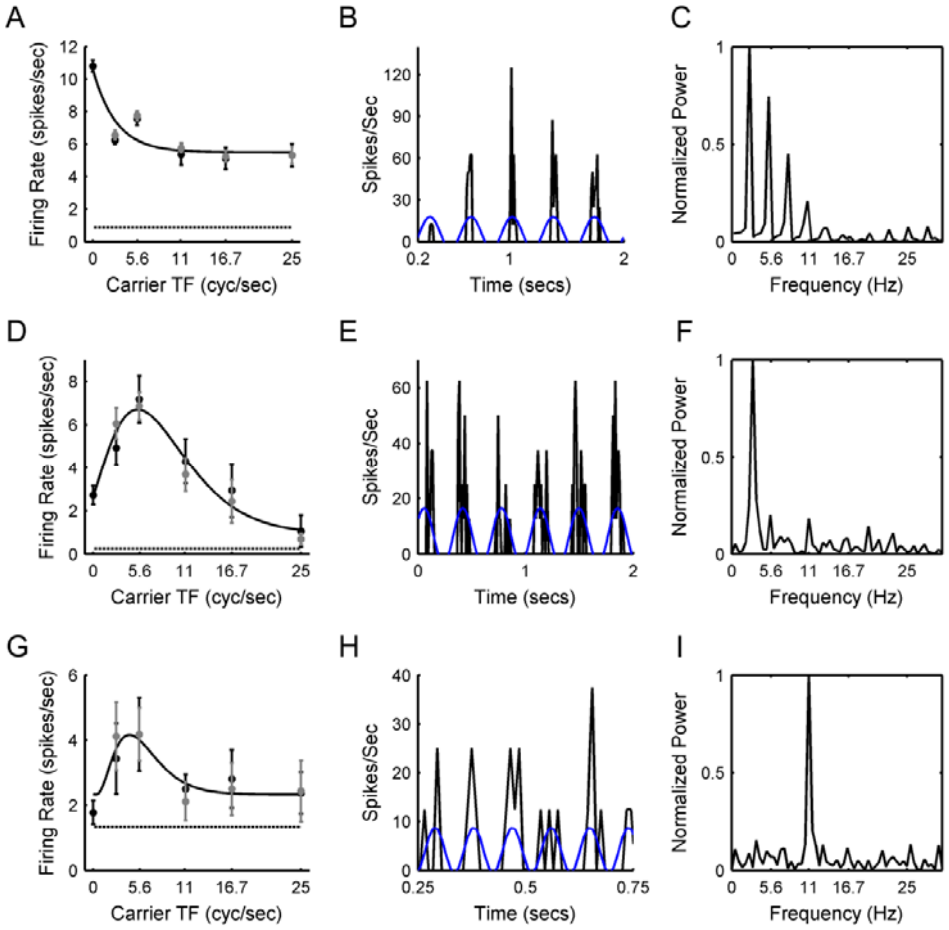

Supplemental Figure 1 Y-cell responses to interference patterns with envelope temporal frequencies other than 5.6 cyc/sec. **(A-C)** Responses of a Y-cell to interference patterns with an envelope TF of 2.8 cyc/sec. **(A)** Carrier TF tuning curve. **(B)** PSTH (black trace) and sinusoidal fit at the envelope TF (blue trace clipped at zero) when the carrier TF was 5.6 cyc/sec. The first 20 msec of the response was excluded because it contained a large transient component. **(C)** Power spectrum of the response shown in **B**. **(D-F)** Responses of a second Y-cell to interference patterns with an envelope TF of 2.8 cyc/sec. **(D)** Carrier TF tuning curve. **(E)** PSTH and sinusoidal fit at the envelope TF when the carrier TF was 5.6 cyc/sec. **(F)** Power spectrum of the response shown in **E**. **(G-I)** Responses of a Y-cell to interference patterns with an envelope TF of 11.1 cyc/sec. **(G)** Carrier TF tuning curve. **(H)** PSTH and sinusoidal fit at the envelope TF when the carrier TF was 5.6 cyc/sec. Only 500 msec of the response are shown so that the oscillations at the envelope TF are more clearly visible. **(I)** Power spectrum of the full 2 sec response partially shown in **H**. (**A,D,G**) Layout as in **Figure 2**. **(C,F,I)** Note that the dominant response frequency was always at the envelope TF. In **C**, response rectification and the narrowness of the PSTH at each stimulus cycle also resulted in power at harmonics of the envelope TF, as observed in **Figure 3**. In **F** and **I**, there was little power at the carrier TF of 5.6 cyc/sec.

Supplemental Figure 2

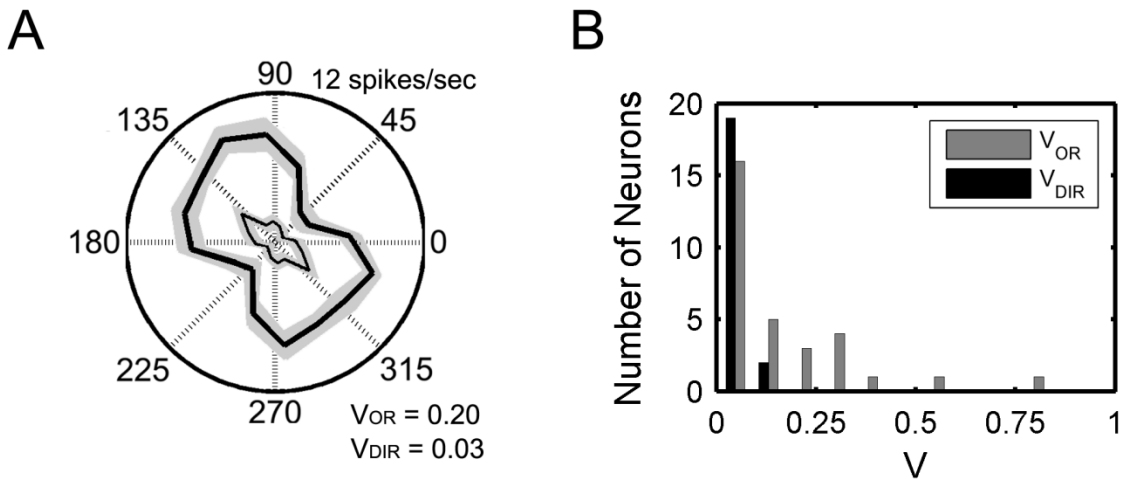

Supplemental Figure 2 Y-cell carrier orientation and direction tuning. **(A)** Carrier orientation and direction tuning for the neuron shown in **Figure 2C**. The tuning curve with the smaller amplitude responses was measured with a static carrier, the carrier TF at which the cell was least responsive (V_{OR} = 0.29). The larger amplitude tuning curve was measured at the peak carrier TF (16.7 cyc/sec). Similar orientations are preferred at either carrier TF. Based on the measurements at the preferred carrier TF, the neuron was not direction selective (V_{DIR} = 0.03) but was moderately orientation selective (V_{OR} = 0.20). Baseline subtracted mean responses are plotted in black and SEM in gray. **(B)** Carrier orientation and direction selectivity measured at the preferred carrier TF. Histogram of carrier orientation selectivity is shown in gray (V_{OR}; N = 31). Histogram of carrier direction selectivity is shown in black (V_{DIR}; N = 21).

Supplemental Figure 3

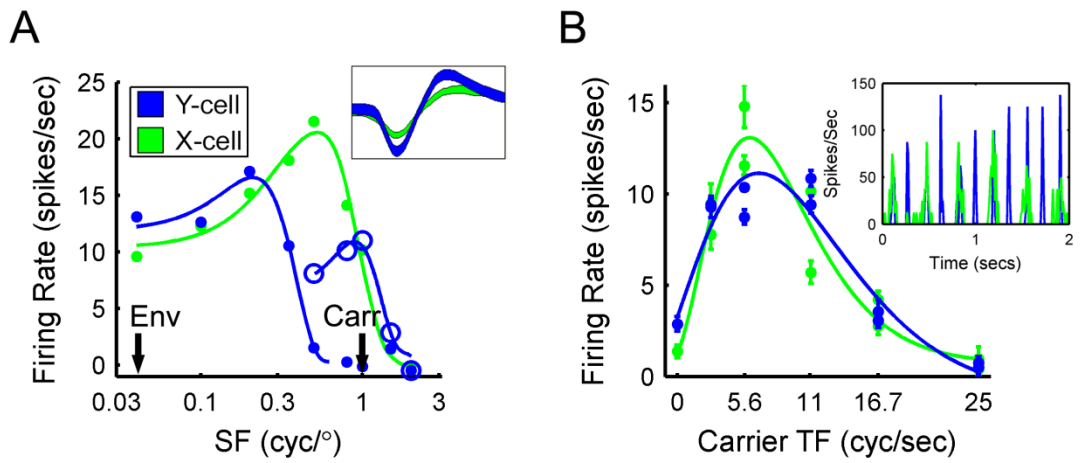

Supplemental Figure 3 Spatiotemporal frequency tuning of a simultaneously recorded X-cell and Y-cell. **(A)** SF tuning curves. The Y-cell SF tuning curves are presented in blue; solid points are mean responses to drifting gratings and open circles are mean responses to contrast-reversing gratings. The X-cell SF tuning curve is presented in green; responses were measured with drifting gratings (same X-cell as in **Figure 4**). The data are baseline subtracted. Solid curves are difference of Gaussians model fits. The interference pattern SF parameter selections are marked with arrows. The inset shows the action potential waveforms for the two cells. **(B)** Carrier TF tuning curves measured for the two cells using the SF parameters marked in **A**. The data are baseline subtracted. The two data points plotted at each non-zero carrier TF are mean responses to interference patterns with carriers drifting in opposite directions. Solid curves are gamma function fits. Although the tuning curves are similar, the temporal responses are quite different. The inset shows PSTHs for the two cells for the same condition. Whereas the response of the Y-cell oscillated predominantly at the envelope TF (5.6 cyc/sec), the response of the X-cell oscillated predominantly at the carrier TF (2.8 cyc/sec).

Supplemental Figure 4

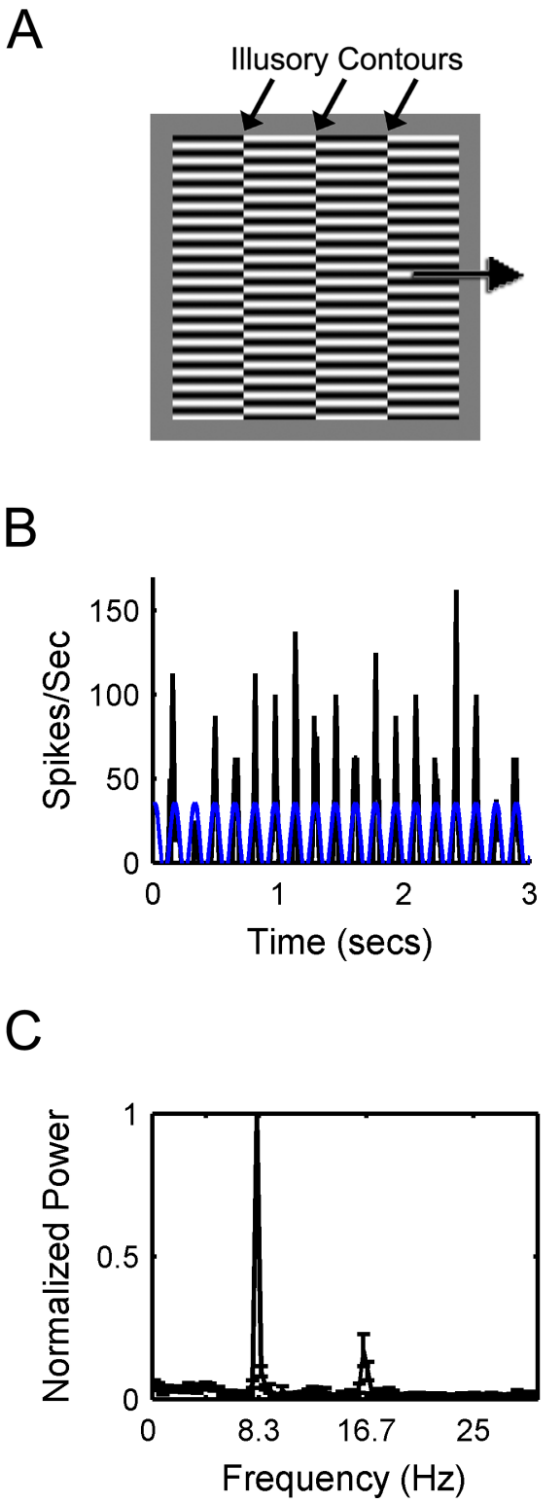

Supplemental Figure 4 Y-cell responses to illusory contours. **(A)** An abutting grating stimulus with a high SF horizontally oriented carrier. Three vertical ICs are perceived (indicated by arrows). In these experiments the ICs drifted (illustrated by the rightward pointing arrow) and the carrier was static. **(B)** The PSTH of a Y-cell response to a drifting abutting grating stimulus is shown in black. The blue trace shows the fit of a sinusoid with the stimulus frequency of 6.3 ICs/sec to the PSTH (fit clipped at zero). **(C)** Average normalized power spectrum of the responses of 2 other Y-cells to a total of 10 abutting grating stimuli which differed in the orientations of the carrier and ICs. Consistent with the output of a demodulating system, the responses oscillated at the frequency of ICs/sec (8.3 Hz). An additional peak is observed at the second harmonic. Mean ± SEM plotted (N = 10).

Supplemental Figure 5

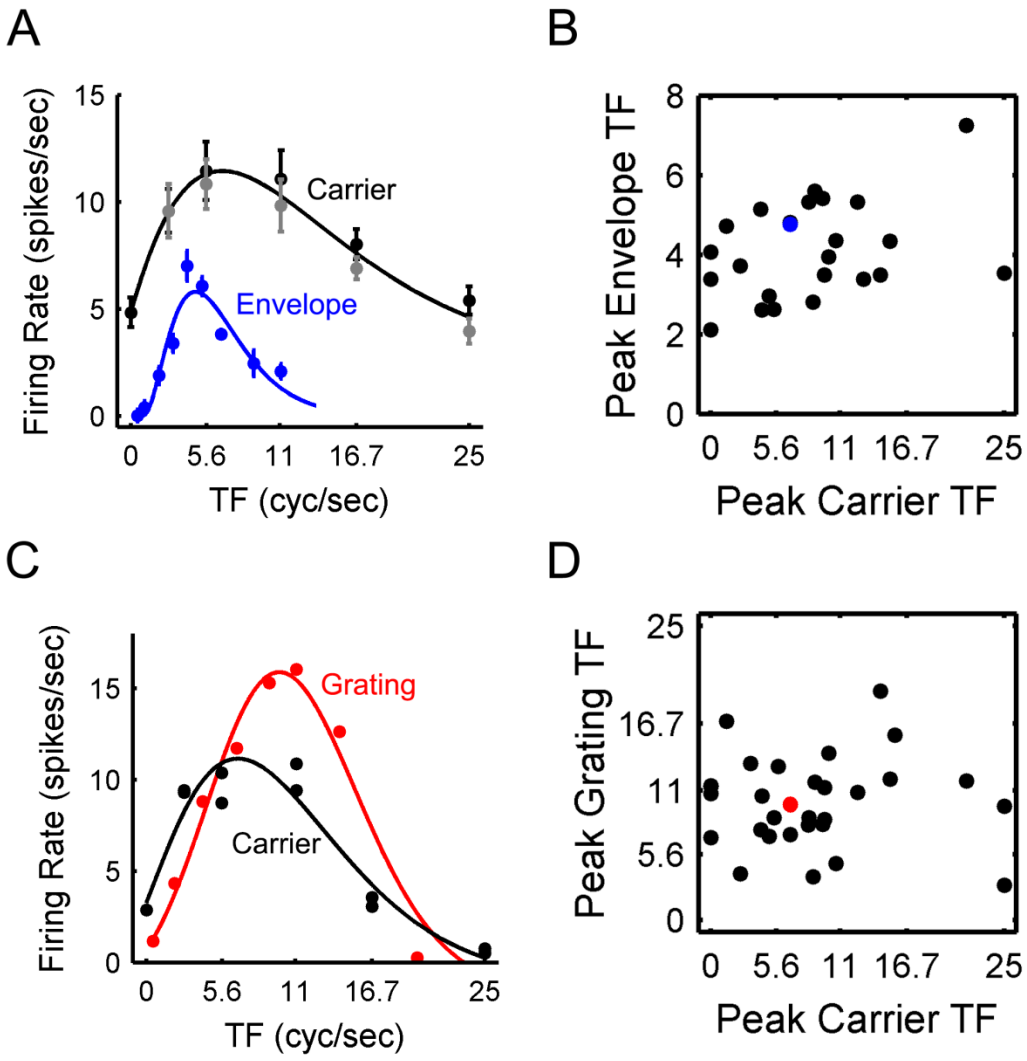

Supplemental Figure 5 Comparisons of Y-cell temporal frequency tuning properties. **(A)** Envelope and carrier TF tuning curves of a Y-cell. Data points are baseline subtracted mean responses and error bars are SEM. For the carrier TF tuning curve, gray and black data points are mean responses to carriers drifting in opposite directions. The envelope TF tuning curve was measured with a static carrier so the maximum response in the envelope TF tuning curve is similar in amplitude to the response to the static carrier in the carrier TF tuning curve. **(B)** Scatter plot of the peak envelope TFs and peak carrier TFs for 24 Y-cells. Blue point corresponds to the neuron in **A**. There was a moderate but non-significant correlation between the peak envelope TFs and peak carrier TFs ($r = 0.36$, $p = 0.08$). **(C)** Grating and carrier TF tuning curves of a Y-cell. For the carrier TF tuning curve, responses to carriers drifting in opposite directions are both plotted in black. Data points are baseline subtracted mean responses. **(D)** Scatter plot of the peak grating TFs and peak carrier TFs for 30 Y-cells. Red point corresponds to the neuron in **C**. There was no correlation between the peak grating TFs and peak carrier TFs ($p = 0.96$).

Supplemental Figure 6

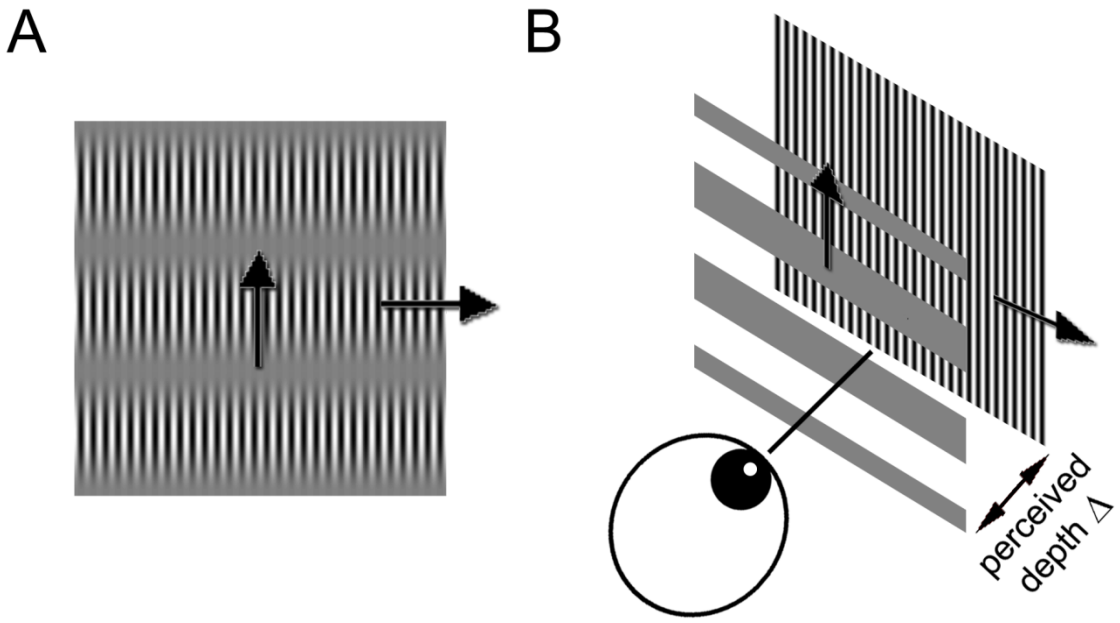

Supplemental Figure 6 The perception of transparent motion elicited by an interference pattern. **(A)** An interference pattern with a horizontally oriented envelope illustrated as drifting upward and a vertically oriented carrier illustrated as drifting rightward. **(B)** Perceptually, the envelope can be seen as drifting in front of (occluding) the moving carrier (Fleet and Langley, 1994).

Supplemental References

Fleet, D.J., and Langley, K. (1994). Computational analysis of non-Fourier motion. Vision Research *34*, 3057-3079.

Rosenberg, A., Husson, T.R., and Issa, N.P. (2010). Subcortical Representation of Non-Fourier Image Features. J. Neurosci. *30*, 1985-1993.